This is a repository copy of *A new quasilinear saturation rule for tokamak turbulence with application to the isotope scaling of transport*.

A new quasilinear saturation rule for tokamak turbulence with application to the isotope scaling of transport

H. G. Dudding,[1,2,*] **F. J. Casson,**[1] **D. Dickinson,**[2] **B. S. Patel,**[1] **C. M. Roach,**[1] **E. A. Belli,**[3] **G. M. Staebler**[3]

[1]Culham Centre for Fusion Energy, Abingdon, Oxfordshire, OX14 3DB, UK
[2]York Plasma Institute, Department of Physics, University of York, Heslington, York, YO10 5DD, UK
[3]General Atomics, P.O. Box 85608, San Diego, California 92186-5608, USA
[*]Email: harry.dudding@ukaea.uk

Abstract

A new quasilinear saturation model SAT3 has been developed for the purpose of calculating radial turbulent fluxes in the core of tokamak plasmas. The new model is shown to be able to better recreate the isotope mass dependence of nonlinear gyrokinetic fluxes compared to contemporary quasilinear models, including SAT2 [1], whilst performing at least as well in other key equilibrium parameters. By first quantifying the isotope scaling of gyrokinetic flux spectra, it is shown that the deviation from the gyroBohm scaling of fluxes originates primarily in the magnitude of the saturated potentials. Using this result SAT3 was formulated using observations made from gyrokinetic data, including a novel and robust relation between the 1D potential spectrum and the radial spectral widths. This serves to define the underlying functional forms of SAT3 before then connecting to the linear dynamics, including a difference in saturation level between ITG- and TEM-dominated turbulence, with the resulting free parameters having been fit to a database of high-resolution nonlinear CGYRO simulations. Additional features outside of the database are included, including $E \times B$ shear and multi-ion plasma capability. The methodology used in the development of SAT3 represents an algorithm which can be used in the improvement and generation of future saturation models.

1 Introduction

In the field of tokamak transport it is well established that the isotope scaling of the global energy confinement time τ_E is not commensurate with that suggested by simple theory [2–5], which assumes that local turbulent fluxes Q_i follow gyroBohm scaling, for which $Q_i \propto \sqrt{A}$ for ion mass number A, and that there exists a simple translation between the local fluxes in the device and the global confinement properties, $\tau_E \propto 1/Q_i \propto A^{-0.5}$. Experimental scaling laws derived from observations made across many tokamaks however consistently observe positive scalings, $\tau_E \propto A^p$, $p > 0$ [6, 7]. Whilst this result bodes well for the success of future tokamak devices in their shift from pure deuterium (D) plasmas to the operational 50/50 mix of deuterium-tritium (DT), the mechanisms responsible for this 'isotope effect' remain incompletely understood.

To investigate the gyroBohm scaling assumption, nonlinear gyrokinetic codes [8–10] can be used to accurately simulate how local turbulent fluxes depend on isotope mass. Previous studies have shown that in sufficiently simple cases, namely those dominated by ITG turbulence with a single ion species and adiabatic electrons, the gyroBohm scaling of fluxes is produced [11, 12]. The inclusion of more sophisticated physics in these simulations breaks this scaling, as has been demonstrated for the inclusion of kinetic electrons [13], electromagnetic effects [14], collisions [15] [16], $E \times B$ shear [17] and fast particles [18]. Numerous studies have also shown that not only can local fluxes deviate from the gyroBohm prediction, but can follow the opposite trend, the so-called anti-gyroBohm scaling, in which fluxes scale inversely with isotope mass [13, 19]. The plurality of mechanisms involved in this gyroBohm-breaking effect makes even a partial explanation of the isotope effect on a local level challenging.

Nonlinear gyrokinetics represents the most accurate plasma turbulence modelling paradigm available, having been extensively validated against experiment [20–27]. However, its great computational expense renders it impractical for use in integrated modelling simulations, in which one is required to simulate many flux surfaces over confinement timescales. Quasilinear models such as TGLF [28] and QuaLiKiz [29] are instead used for this purpose. These models bypass the expense of calculating the fluxes in the nonlinear gyrokinetic system by instead solving for the linear response of the plasma instabilities, which is then combined with an estimation of the magnitude of the saturated potentials via a saturation rule to provide a calculation of the fluxes in a greatly reduced time. A standard and relatively simple estimation of these potential magnitudes comes from the mixing length rule [29], which models the

turbulent transport as a diffusive process, with a step size of a characteristic wavenumber of the linear instability and a time step of the inverse of the growth rate. This estimation is employed in QuaLiKiz [30], however saturation rules can be based on other turbulence saturation mechanisms, such as TGLF SAT1 [31] and SAT2's [1] paradigm of zonal mixing. Quasilinear models have been extensively validated against nonlinear gyrokinetic codes for deuterium plasmas [1, 32] and have successfully modelled deuterium plasma discharges [11, 33–36]. However, their historically limited considerations of plasmas in other isotopes, coupled with their incomplete description of the isotope effect, cause them to struggle to replicate the behaviour of nonlinear gyrokinetic fluxes with isotope mass, rendering predictive flux-driven modelling efforts unreliable [11, 19].

An example of the isotope effect as it appears in local nonlinear gyrokinetics was explicitly demonstrated in a paper by E. A. Belli *et al* [13], focusing on the role of kinetic electrons. It was shown using the gyrokinetic code CGYRO [9] that by increasing the equilibrium density gradient from a GA-standard case [37] baseline, one moves from a regime of ITG-dominated turbulence to TEM-dominated turbulence, accompanied by a reversal in the flux scaling. It was suggested that this anti-gyroBohm scaling may not be captured by reduced turbulence models, in part due to the observation that the mixing length rule did not exhibit this isotope reversal.

To test the adherence between the nonlinear (NL) CGYRO results and the quasilinear model results, the NL CGYRO data from the density gradient scan presented in [13] is shown in figure 1, along with the data from equivalent simulations using TGLF-SAT1, TGLF-SAT2 and QuaLiKiz. Moving from $a/L_n = 0.0$ to $a/L_n = 3.0$, one observes that the anti-gyroBohm scaling seen in the data from NL CGYRO for $a/L_n > 2.0$ is not replicated in the results of any of the three quasilinear models. These all instead exhibit positive isotope scaling across the scan, indicating that the relevant physics to capture this isotope scaling reversal is missing.
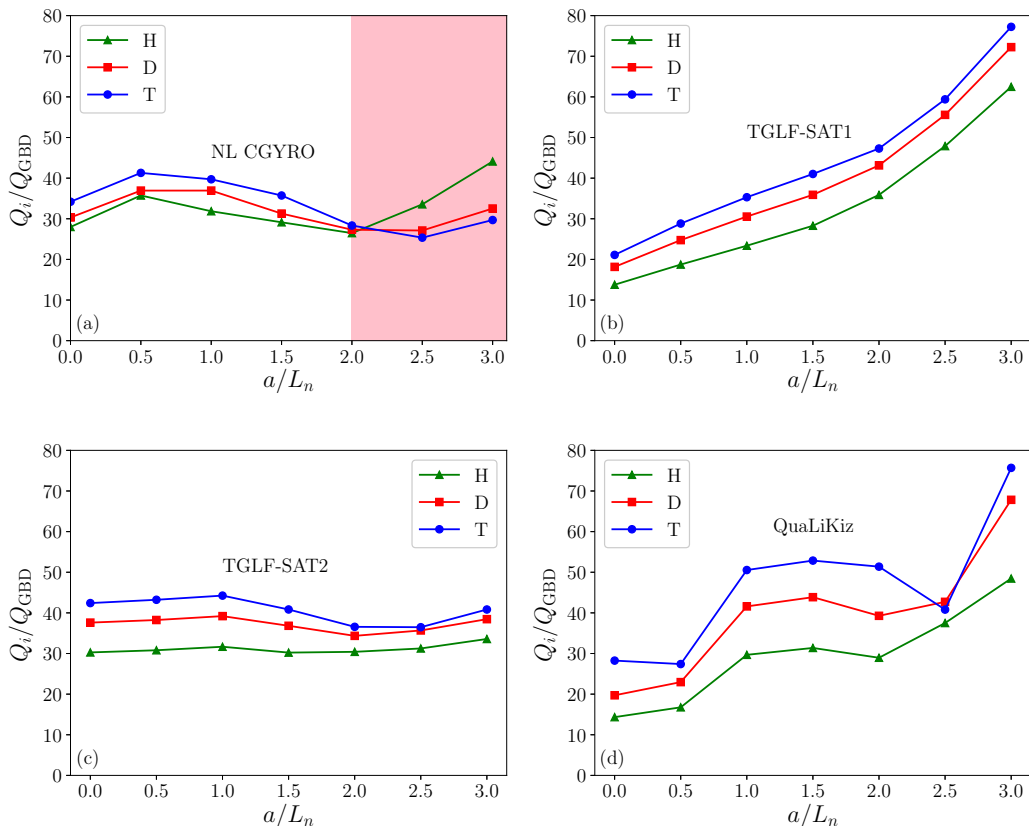

Figure 1: Turbulent ion energy fluxes against density gradient scale length for (a) NL CGYRO, (b) TGLF-SAT1, (c) TGLF-SAT2 and (d) QuaLiKiz in H, D and T, from a GA-std case baseline. Note that the isotope scaling reversal present in NL CGYRO (shaded region) is not recreated in any of the quasilinear models. Subfigure (a) reproduced from [13], with the permission of AIP Publishing.

The inability of current models to reliably predict this scaling undermines the efforts of integrated modelling in terms of prediction and optimisation of experimental campaigns in plasmas with compositions differing from pure deuterium. With the advent of ITER and the subsequent shift to operations with DT, as well as isotope experiments at the JET tokamak, it is essential that modern quasilinear models more accurately approximate fluxes in different isotopes.

The aim of this work is to develop a new quasilinear model that is able to more reliably predict how turbulent fluxes scale with isotope mass, by capturing the physics contained in local nonlinear gyrokinetic simulations. The paper is organised as follows: Section 2 contains a discussion on the theory of turbulent plasma fluxes, and how this informs the structure of quasilinear models. The detail of the gyrokinetic database created for this work is given in Section 3. In Section 4, contemporary reduced transport models are compared with gyrokinetic simulations, to illustrate in detail how those models fail to capture the isotope dependence of the transport. Section 5 describes the development of the new saturation rule SAT3, with a summary of the model given in Section 5.7, and Section 6 presents the results from SAT3. A conclusion follows.

2 Turbulent fluxes

2.1 Fluxes in gyrokinetics

The following employs local flux-tube geometry [38] with coordinates $\{x, y, \theta\}$ denoting the radial, binormal and parallel-to-field coordinates respectively. A summary of the field-aligned system, geometric conventions and averages used in this paper is given in Appendix A. This work focuses primarily on electrostatic turbulence, such that the only non-negligible component of the turbulent electromagnetic field is the fluctuating electrostatic potential $\delta\phi$.

Turbulent heat fluxes arise in the gyrokinetic system due to the interaction between $\delta\phi$ and the pressure fluctuations of the present plasma species δp_s (for species s) via the turbulent $E \times B$ velocity [39, 40]. Once saturated, a statistically steady-state flux can be defined by taking both an ensemble average and a flux-surface average over these fluctuations. Of particular interest is the radial component of this averaged flux, due to its integral role in determining the confinement properties of the plasma. This is given by

$$Q_s = \left\langle \nabla x \cdot \frac{\hat{\mathbf{b}} \times \nabla \delta\phi}{B} \delta p_s \right\rangle_{\text{Ens,FS}} \tag{1}$$

where $\hat{\mathbf{b}}$ is the unit vector in the direction of the equilibrium magnetic field, $B = |\mathbf{B}|$ is the equilibrium magnetic field magnitude, and $\langle...\rangle_{\text{Ens,FS}}$ denotes an average over the turbulent ensemble and flux-surface respectively. By representing each fluctuating quantity as a Fourier series in x and y, one can show that equation 1 may be written (a step-by-step derivation is given in Appendix B):

$$Q_s = \sum_{k_y > 0} 2 \sum_{k_x} \left\langle \frac{k_y \text{Im}\left[Z^*_{s,k_x,k_y}\right]}{B_{\text{unit}}} \left|\delta\hat{\phi}_{k_x,k_y}\right|^2 \right\rangle_{\theta,t}$$
$$= \sum_{k_y > 0} Q_{s,k_y} \tag{2}$$

where $Z_{s,k_x,k_y} = \delta\hat{p}_{s,k_x,k_y} / \delta\hat{\phi}_{k_x,k_y}$. Here the total flux Q_s has been decomposed into a sum of discrete flux components per positive binormal wavenumber, $Q_{s,k_y} = 2\sum_{k_x} \left\langle \frac{k_y \text{Im}\left[Z^*_{s,k_x,k_y}\right]}{B_{\text{unit}}} \left|\delta\hat{\phi}_{k_x,k_y}\right|^2 \right\rangle_{\theta,t}$. Circumflexes are used to denote Fourier amplitudes and * signifies a complex conjugate. The averages over θ and t are defined by equations A.5 and A.6, and B_{unit} is an effective magnetic field

$$B_{\text{unit}} = \frac{q(r)}{r} \frac{\text{d}\psi}{\text{d}r} \tag{3}$$

where ψ is the poloidal magnetic flux divided by 2π, q is the safety factor and r denotes a given flux-surface.

Equation 2 shows that each flux component Q_{s,k_y} can be considered as a sum over k_x of averaged terms comprised of two factors: the squared magnitude of the potential fluctuations $\left|\delta\hat{\phi}_{k_x,k_y}\right|^2$, and $k_y \text{Im}\left[Z^*_{s,k_x,k_y}\right] / B_{\text{unit}}$, which contains the phase difference between the pressure and potential fluctuations.

2.2 Fluxes in reduced models

Two types of reduced turbulence models are considered in this work: Those with 'exact' linear solvers, which compute the linear behaviour of microinstabilities using a local gyrokinetic code, and those with 'fast' linear solvers, which solve a simplified version of the linear gyrokinetic system to approximate the linear response of the plasma in a greatly reduced time. The results of these solvers are then combined with a saturation rule in order to calculate turbulent fluxes.

Whilst the use of exact linear solvers is too computationally expensive for routine use in reduced models required by integrated modelling, it is useful for the purposes of saturation rule development, as the dynamics of the linear microinstability are computed more accurately. This model type has been used previously [41–43], including under the name 'QLGYRO' [44], for which linear CGYRO results were combined with TGLF's SAT1 rule. In the interest of generality, in this paper reduced models will be referred to using the taxonomy ⟨ linear inputs ⟩-⟨ saturation rule ⟩, to clearly specify the constituents of each model. Thus CGYRO-SAT1 refers to the QLGYRO paradigm, TGLF-SAT1 refers to SAT1 with the reduced linear inputs of TGLF, and the QuaLiKiz saturation rule (qlk) with the linear inputs of QuaLiKiz is QuaLiKiz-qlk.

The flux calculation of models using an exact linear solver will first be considered. For each k_y one can define an average phase, dubbed the 'weight' W_{s,k_y}, such that

$$W_{s,k_y} = \left\langle \frac{k_y \mathrm{Im}\left[Z^*_{s,k_x,k_y}\right]}{B_{\mathrm{unit}}} \right\rangle = \frac{\sum_{k_x} \left\langle \frac{k_y \mathrm{Im}\left[Z^*_{s,k_x,k_y}\right]}{B_{\mathrm{unit}}} \left|\delta\hat{\phi}_{k_x,k_y}\right|^2 \right\rangle_{\theta,t}}{\sum_{k_x} \left\langle \left|\delta\hat{\phi}_{k_x k_y}\right|^2 \right\rangle_{\theta,t}} = \frac{\frac{1}{2} Q_{s,k_y}}{\left\langle \left|\delta\hat{\phi}_{k_y}\right|^2 \right\rangle_{x,\theta,t}} \tag{4}$$

where the relation

$$\left\langle \left|\delta\hat{\phi}_{k_y}\right|^2 \right\rangle_{x,\theta,t} = \sum_{k_x} \left\langle \left|\delta\hat{\phi}_{k_x,k_y}\right|^2 \right\rangle_{\theta,t} \tag{5}$$

is a consequence of Parseval's theorem (Appendix C). Note the factor of $\frac{1}{2}$ in the final expression of the weights due to historical convention. One can define both a 'nonlinear weight' W^{NL}_{s,k_y} and a 'linear weight' W^{L}_{s,k_y}, named due to their calculation from the nonlinear gyrokinetic system and the linear gyrokinetic system respectively. The flux obtained from nonlinear gyrokinetics may therefore be written as a 1D sum over binormal wavenumber of nonlinear weights and potentials:

$$Q_s = 2 \sum_{k_y>0} W^{\mathrm{NL}}_{s,k_y} \left\langle \left|\delta\hat{\phi}_{k_y}\right|^2 \right\rangle_{x,\theta,t} \tag{6}$$

To express the flux in a form relevant to reduced models, and assuming only the dominant mode is considered in the linear solver, one multiplies and divides by the linear weight:

$$\begin{aligned} Q_s &= 2 \sum_{k_y>0} \left[\frac{W^{\mathrm{NL}}_{s,k_y}}{W^{\mathrm{L}}_{s,k_y}}\right] W^{\mathrm{L}}_{s,k_y} \left\langle \left|\delta\hat{\phi}_{k_y}\right|^2 \right\rangle_{x,\theta,t} \\ &= 2 \sum_{k_y>0} \Lambda_{s,k_y} W^{\mathrm{L}}_{s,k_y} \left\langle \left|\delta\hat{\phi}_{k_y}\right|^2 \right\rangle_{x,\theta,t} \end{aligned} \tag{7}$$

where $\Lambda_{s,k_y} = W^{\mathrm{NL}}_{s,k_y}/W^{\mathrm{L}}_{s,k_y}$ is the 'quasilinear approximation (QLA) function'. This defines an explicit measure of the quasilinear approximation, which assumes that the average phase between the fluctuations in the linear regime is conserved in the nonlinear regime [45]. If this approximation were to be satisfied exactly, one would observe $\Lambda_{s,k_y} = 1$ for all species at all binormal wavenumbers, which is typically assumed in current quasilinear models.

Finally, for the purposes of reduced modelling, one does not mathematically describe the potentials $\left\langle \left|\delta\hat{\phi}_{k_y}\right|^2 \right\rangle_{x,\theta,t}$, but rather the potentials normalised to the binormal grid spacing Δk_y, as this can be shown to be invariant under a change of grid resolution once past the point of convergence (Appendix D). This consideration yields

$$Q_s = 2 \sum_{k_y>0} \Lambda_{s,k_y} W^{\mathrm{L}}_{s,k_y} \left[\frac{\left\langle \left|\delta\hat{\phi}_{k_y}\right|^2 \right\rangle_{x,\theta,t}}{\Delta k_y}\right] \Delta k_y \tag{8}$$

which is the final result for the structure of fluxes in quasilinear models with an exact linear solver. Each term in the sum over k_y is comprised of four parts, two of which are obtained from linear simulations, and two of which must be prescribed. The two linearly determined quantities are the adopted binormal grid spacing Δk_y and the linear weight, W^{L}_{s,k_y}. The two quantities in need of prescription are the grid-independent potentials $\left\langle \left| \delta \hat{\phi}_{k_y} \right|^2 \right\rangle_{x,\theta,t} / \Delta k_y$, calculated by the quasilinear saturation rule, and the QLA function, Λ_{s,k_y}.

The flux calculation for the fast model type is similar to equation 8, however as they solve a simplified version of the linear gyrokinetic system, some additional sources of error are incurred due to their approximate calculation of the linear response. These errors can enter through the linear weights and through linear quantities needed in the saturation rule, typically the growth rate of the dominant mode.

Note that the discussion and derivations in this section thus far hold completely analogously for the particle flux Γ_s and momentum flux Π_s, by simply substituting the pressure fluctuations δp_s for the density fluctuations δn_s or velocity fluctuations δv_s respectively in equation 1.

3 Simulation database

Normalising quantities in this work are given in SI units. These normalisations are the deuterium mass m_D, the electron temperature T_e, the electron density n_e, the tokamak minor radius a and the effective magnetic field B_{unit}, defined by equation 3. The reference gyroradius is therefore $\rho_{\mathrm{unit}} = \sqrt{m_D T_e}/e B_{\mathrm{unit}}$, with $\rho_* = \rho_{\mathrm{unit}}/a$, and the deuterium sound speed is $c_s = \sqrt{T_e/m_D}$. Other useful normalisations include those of frequency c_s/a, particle flux $\Gamma_{\mathrm{GBD}} = \rho_*^2 n_e c_s$, energy flux $Q_{\mathrm{GBD}} = \rho_*^2 n_e T_e c_s$ and the electrostatic potential $\phi_{\mathrm{unit}} = \rho_* T_e/e = B_{\mathrm{unit}} \rho_{\mathrm{unit}}^2 (c_s/a)$.

A database of 43 nonlinear gyrokinetic simulations was generated using CGYRO [9]. The database is primarily centered around the GA-std case, defined by $a/L_{T_i} = a/L_{T_e} = 3.0$, $a/L_n = 1.0$, $T_i/T_e = 1.0$, $\hat{s} = 1.0$, $q = 2.0$, $(a/c_s)\nu_{ee} = 0.1$ and circular Miller flux-surface geometry with $r_0/R_0 = 1/6$, for tokamak major radius R_0. Definitions of equilibrium geometry quantities correspond to those found in [46]. Kinetic electrons and a single ion species are used for all cases. The three isotopes that have been simulated are H, D and T, with m_i/m_D values of $0.5, 1.0$ and 1.5 respectively. No rotation is included. All simulations are predominantly electrostatic, however include $\delta A_\parallel$ fluctuations with a small plasma beta of $\beta_{e,\mathrm{unit}} = 0.05\%$ to allow for an increased time-step with negligible effect on the fluxes [9]. Additional parameters considered include the elongation κ and the Shafranov shift $\Delta = dR_0/dr$, and w is the box size integer which relates the radial and binormal domains, $L_x = L_y w/(2\pi \hat{s})$. Changes in temperature gradient scale lengths were kept constant between the ions and electrons ($a/L_{T_i} = a/L_{T_e}$). In table 1, the tokamak parameters that differ from the GA-std baseline are shown for the database.

The resolutions used in this work for the nonlinear simulations are $N_y = 40$ binormal modes, $N_x = 224$ radial modes, $N_\theta = 32$ parallel grid-points, $N_\xi = 16$ pitch-angle grid-points and $N_u = 8$ energy grid-points. The density of binormal modes is greater than that typically used in studies of similar cases [13], as it was found during convergence tests that this lower resolution can cause fluxes to be under-predicted. The box size integer w has a value of 4 for all simulations except those changing the magnetic shear from its baseline value of $\hat{s} = 1$. For these cases, the box length integer was also changed so as to keep $\hat{s}/w$ constant and thus the radial domain length unchanged. All simulations were conducted at the ion scale up to $k_y \rho_i = 1.0$, where $\rho_i = \sqrt{m_i/m_D}\rho_{\mathrm{unit}}$, to keep the radial and binormal domains constant relative to the main ion gyroradius. This binormal grid set-up was also used for the quasilinear model simulations of TGLF and QuaLiKiz shown in figure 1. Finite aspect-ratio Miller geometry was used for all simulations other than those of QuaLiKiz, which used large aspect-ratio circular geometry.

Nonlinear simulations were given sufficient time to saturate, running to at least $(c_s/a)\tau > 1000$, where τ is the total simulation time. Time averages of fluctuating data were performed by taking three separate measurements with consecutive time-windows of size 0.28τ between 0.16τ and τ. From these three measurements a mean and standard deviation were calculated for the final result. These windows were chosen to avoid the initial linear regime of the simulations, and to provide a representative standard deviation of the statistical fluctuations. Unless otherwise noted, all error bars shown in this work are the standard deviations obtained from this method.

For each nonlinear case 39 linear simulations were also conducted, corresponding to the 39 non-zero binormal modes present in their respective nonlinear simulations. An altered radial domain was used with $N_x = 128$ and $w = 1$, due

Varied Parameter	Values (Label)	Fixed	Isotopes Simulated
- (GA-std)	- (a)	-	H, D, T
$a/L_{T_i} = a/L_{T_e}$	1.5 (b), 2.25 (c), 3.5 (d)	-	H, D, T
a/L_n	2.0 (e), 3.0 (f)	-	H, D, T
$\hat{s}$	0.25 (g), 0.5 (h), 1.5 (i)	$\hat{s}/w = 1/4$	D
$(a/c_s)\nu_{ee}$	0.01 (j)	-	H, D, T
$(a/c_s)\nu_{ee}$	1.0 (k)	-	D
T_i/T_e	0.5 (l), 1.5 (m)	-	D
q	1.5 (n), 2.5 (o)	-	D
κ	1.25 (p), 1.5 (q), 2.0 (r)	-	D
Δ	-0.125 (s), -0.25 (t), -0.5 (u)	-	D
r_0/R_0	1/4 (v), 1/12 (w)	-	D
$(a/c_s)\nu_{ee}$	0.01 (x)	$a/L_n = 3.0$	H, D, T
$(a/c_s)\nu_{ee}$	0.05 (y)	$a/L_n = 3.0$	H, T
$(a/c_s)\nu_{ee}$	1.0 (z)	$a/L_n = 3.0$	D

Table 1: Details of the 43 nonlinear CGYRO simulations that form the database. Note that the labels in the second column correspond with those in figure 13(c), used for discerning the cases displayed in figures 13(a), 13(b), 17 and 18.

to the difference in grid requirements for convergence between nonlinear and linear runs.

A single nonlinear simulation of the GA-std case in D was repeated with $N_x = 896$ keeping $w = 4$, for use in figure 7. This extended domain case plays no other part in the work.

Six additional linear simulations were also performed scanning over relative concentrations of D and T in mixed DT plasmas for the GA-std and $a/L_n = 3.0$ cases in Section 5.5.2. The values simulated are $n_D/n_e = \{0.25, 0.5, 0.75\}$, with $n_T/n_e = 1 - n_D/n_e$.

4   Model comparison and isotope scaling diagnosis

In this section, the results from the CGYRO database are compared with those obtained from CGYRO-SAT1, TGLF-SAT1 and QuaLiKiz-qlk[1]. This is done to observe from where in the nonlinear gyrokinetic data the non-trivial isotope scaling originates, as per the flux breakdown in equation 8, as well as to identify why the current reduced models are not reproducing the NL CGYRO results. As an example case this section will focus on the three $a/L_n = 3.0$ simulations, due to the anti-gyroBohm scaling present in the fluxes.

To analyse the isotope scaling of these models the metric α_A is introduced, such that for flux data in H, D and T, one may fit the data with a function of the form

$$f(A; C_A, \alpha_A) = C_A A^{\alpha_A} \tag{9}$$

where the values of C_A and α_A are found via best fit to the data points. An advantage to this metric is that one number α_A describes the isotope scaling for three isotopes, whereas previously used metrics [11, 17] have been based around taking the difference between two fluxes, and thus at least two numbers have been needed for an approximately equivalent description. The values of α_A are also intuitive: if one measures an α_A value of $\alpha_A \approx 0.5$, one knows that the case follows approximate gyroBohm scaling. If one measures $\alpha_A \approx 0.0$, then the fluxes do not vary with isotope, and for $\alpha_A < 0.0$, the case exhibits anti-gyroBohm scaling. Outside of these limiting cases, one can quantify to what degree the case diverges from gyroBohm scaling: for two hypothetical cases of $\alpha_A = 0.4$ and $\alpha_A = 0.1$, then both

---
[1]The results of TGLF-SAT2 are included in figure 2 only. The behaviour of SAT2 with isotope mass is very similar to that of SAT1, as demonstrated by the similarities in scaling metric between the fluxes of TGLF-SAT1 and TGLF-SAT2 in figure 2. This is in part due to the lack of consideration of isotopes other than deuterium in their development, as well as the similarity of their saturated potentials' functional form. Beyond figure 2 therefore only the results of SAT1 are shown, with any conclusions regarding the isotope scaling of SAT1 also applicable to SAT2.

exhibit positive scaling, however the second 'deviates more' from gyroBohm than the first, by a defined quantitative amount.

Figure 2 shows the total ion energy fluxes for the GA-std case and the $a/L_n = 3.0$ case against A for the four models, as well as TGLF-SAT2. Fitted to each data set is the result of the metric fit with the measured values of α_A displayed in the legend. Positive isotope scaling is seen in the GA-std case (figure 2(a)) for all 5 models, as one would expect for ITG-dominated turbulence representative of the quasilinear models' training datasets[2]. QuaLiKiz remains close to the gyroBohm result.

For the $a/L_n = 3.0$ case, anti-gyroBohm scaling is observed in the NL CGYRO data, whereas the three fast quasilinear models all continue to exhibit positive isotope scaling, $\alpha_A > 0$. For CGYRO-SAT1 one finds $\alpha \approx 0.0$, implying that the use of the linear solver of CGYRO compared with the reduced linear solver of TGLF is having an influence on the isotope scaling. As an exact linear solver type model, the resulting difference in isotope scaling between CGYRO-SAT1 and NL CGYRO can only come from either the QLA function, which is assumed to be constant in SAT1, and/or the functional form of the saturation rule.
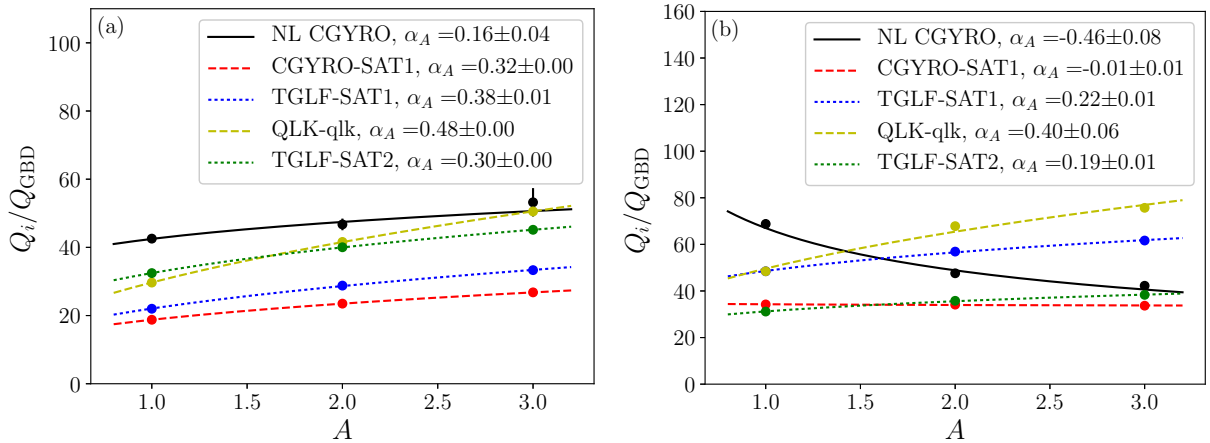

Figure 2: Turbulent ion energy flux against isotope mass for the GA-std case (a) and the $a/L_n = 3.0$ case (b), for NL CGYRO (black), CGYRO-SAT1 (red), TGLF-SAT1 (blue), QuaLiKiz-qlk (yellow) and TGLF-SAT2 (green). Note the positive isotope scaling observed in both cases for the three fast quasilinear models, and the difference between the CGYRO-SAT1 and the TGLF-SAT1 results, originating solely from a difference in linear solver.

To probe this discrepancy further, the decomposition of the total fluxes into their flux components Q_{s,k_y} for the $a/L_n = 3.0$ case is shown in figure 3(a). Here the flux components for NL CGYRO are plotted against $k_y\rho_i$ for the three isotope simulations, such that they have a shared k_y-axis. To quantify the isotope scaling of these flux components the isotope scaling metric α_A can again be used, however now as a function of $k_y\rho_i$, to quantify how the scaling of the flux components varies across the spectrum. Hence for each value of $k_y\rho_i$, the three flux component data points are fitted using equation 9 with the resulting α_A measurements forming an 'α_A line', as shown in black in figure 3(b). This exercise is repeated for CGYRO-SAT1, TGLF-SAT1 and QuaLiKiz-qlk. Also shown in figure 3(b) is a reference line at $\alpha_A = 0.5$, corresponding to the expected result if the flux components followed gyroBohm scaling.

For the NL CGYRO α_A line, the isotope scaling is not uniform across the spectrum as one may expect, but instead two key features can be observed: an 'offset' from the gyroBohm value, most obviously seen in the region of $k_y\rho_i > 0.3$, and a variation in the isotope scaling with $k_y\rho_i$ between $0.0 < k_y\rho_i < 0.3$. It is also in this low k_y region that the flux component magnitudes are largest, and hence contribute most to the total flux and its isotope scaling. Upon consideration of the other cases in the database these features can be shown to be general, with differing offsets and degrees of steepness in the low k_y region. Because the larger $k_y\rho_i$ region's flux contribution is essentially negligible in comparison, figure 3 implies that to accurately capture the isotope scaling of the total flux, one must capture the

---

[2]The difference in magnitude between NL CGYRO and the quasilinear models is due to the increase in the NL CGYRO fluxes compared to previous datasets [1, 31], from the finer grid-resolutions used in this work.
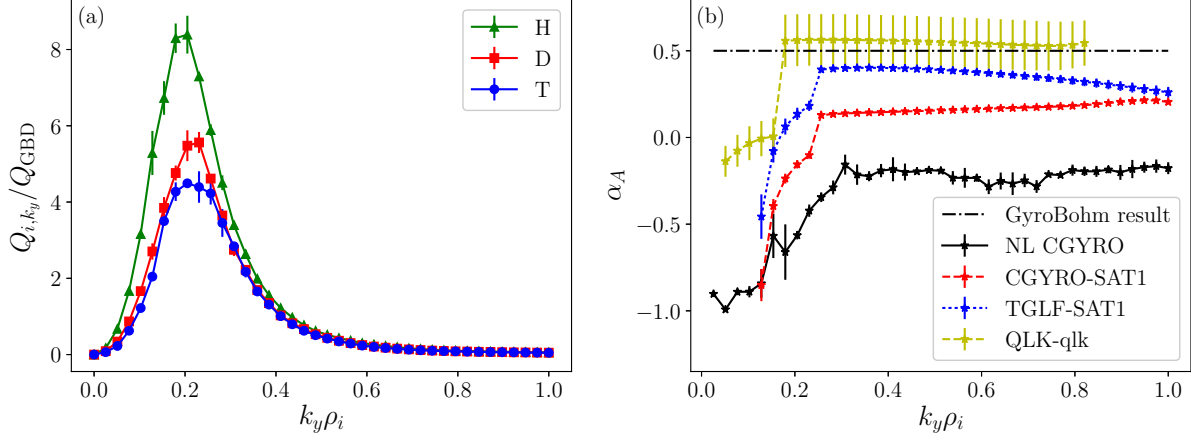
Figure 3: NL CGYRO ion flux components against wavenumber normalised to the main ion gyroradius $k_y\rho_i$ for the $a/L_n = 3.0$ case in H, D and T (a). In (b), the result of applying the α_A metric at each $k_y\rho_i$ is shown for the four models, as well as the value that would be seen if the fluxes followed gyroBohm scaling ($\alpha_A = 0.5$). The error bars shown for all models in (b) are the uncertainties in the fitted parameter α_A.

shape of the flux component spectrum around the peak, as well as the isotope scaling characteristics observed in the low k_y region of the NL CGYRO data of figure 3(b).

Considering now the constituents of the flux components relevant to reduced models, as per equation 8, the two quantities in need of prescription are the QLA functions and the potentials. The results of analogous α_A fitting exercises are shown in figures 4 and 5 for the ion energy QLA function and the saturated potentials respectively, along with their reference lines expected from gyroBohm scaling arguments. Looking at the α_A line of the QLA function in figure 4(b), a small variation of $\alpha_A \sim -0.1$ is seen in the region of low k_y. Reduced models are not shown on this plot as they all assume the QLA function to be exactly 1, and so would be simply aligned with the gyroBohm-predicted result of $\alpha_A = 0.0$.
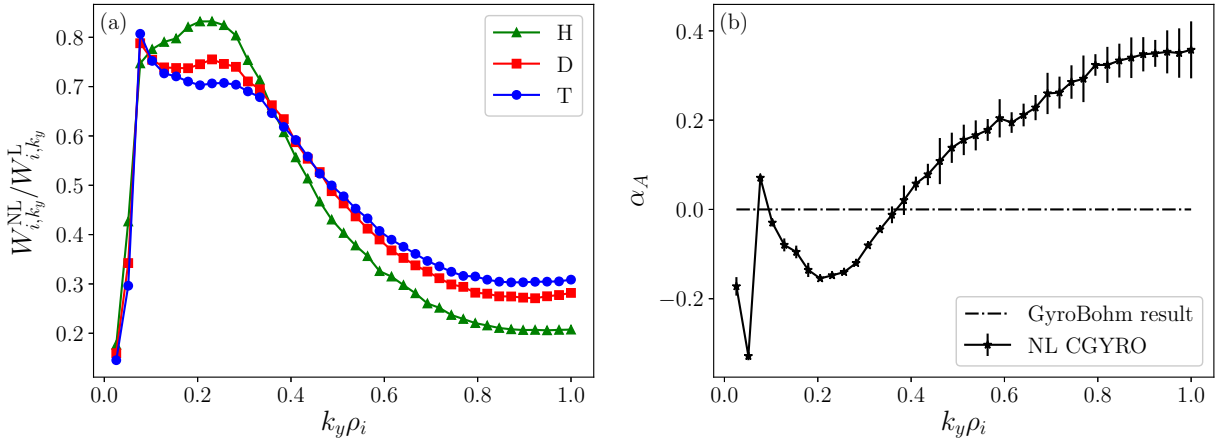

Figure 4: CGYRO ion energy QLA function against $k_y\rho_i$ for the $a/L_n = 3.0$ case in H, D and T (a). In (b), the result of applying the α_A metric at each k_y is shown, including the reference value one would expect if gyroBohm scaling were followed ($\alpha_A = 0.0$). This value is expected as the scaling of the linear and nonlinear weights is the same, $W^{\mathrm{L}}, W^{\mathrm{NL}} \propto e^2 n_e c_s/T \propto A^{-0.5}$, and thus their ratio cancels any predicted scaling dependence. The results of the quasilinear models are not shown as their QLA functions are taken to be constant, and thus exhibit no scaling ($\alpha_A = 0.0$). The error bars shown for the NL CGYRO data in (b) are the uncertainties in the fitted parameter α_A.

8

Whilst there is some non-trivial isotope scaling in the low k_y region of the QLA function, this can be seen to be relatively small when compared to the difference between the NL CGYRO result and the gyroBohm-predicted scaling of the saturated potentials, shown in figure 5(b). The crucial variation in isotope scaling in the low k_y region observed in the flux components is also seen to originate here. Hence for this case, the deviation from gyroBohm scaling of total fluxes in nonlinear gyrokinetics originates primarily in the saturated potentials, specifically in the region of low k_y. Upon consideration of the database more broadly this can be shown to be a general result for the dataset.
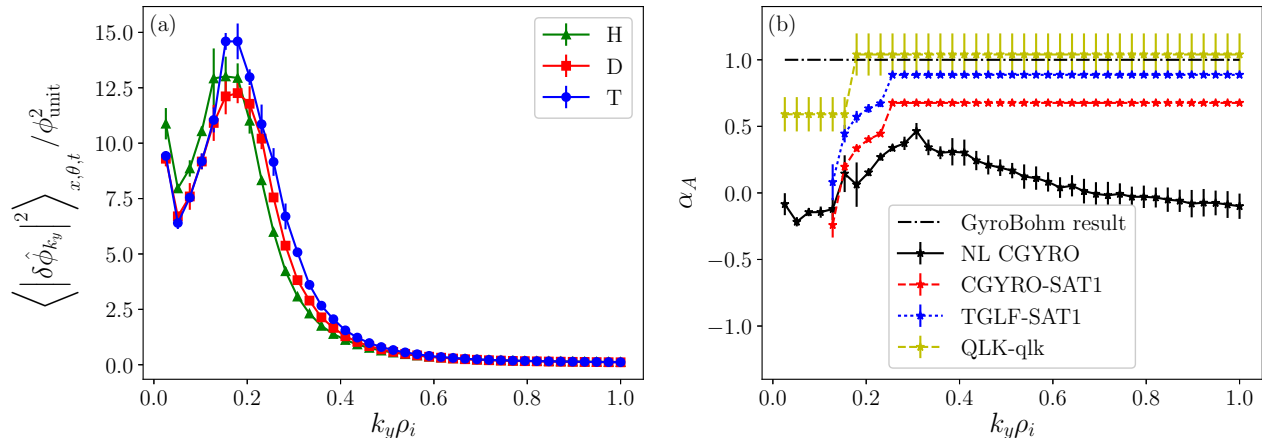

Figure 5: NL CGYRO squared potential magnitudes against $k_y\rho_i$ for the $a/L_n = 3.0$ case in H, D and T (a). In (b), the result of applying the α_A metric at each k_y is shown, including the reference value one would expect if gyroBohm scaling were followed ($\alpha_A = 1.0$), originating from the ordering assumption $\delta\phi^2 \propto \rho_*^2(T/e)^2 \propto A$. The error bars shown for all models in (b) are the uncertainties in the fitted parameter α_A.

Turning to the results of the current quasilinear models in figure 5(b), TGLF-SAT1 and CGYRO-SAT1 both appear to recreate a portion of the isotope scaling variation in the low k_y region, indicating a reasonably accurate spectral shape for SAT1. This implies that it is their offsets that are primarily responsible for the total flux scalings seen in figure 2(b), with the different values attributed to the difference in linear solver. QuaLiKiz-qlk on the other hand does not exhibit this continuous variation, due to the comparatively simple functional form of its spectral shape. The majority of the scaling in the higher k_y region can also be seen to approximately lie at the gyroBohm level for the potentials. These results indicate that neither SAT1 or the QuaLiKiz saturation rule are fully capturing the relevant physics that describes the variation in the saturated potentials with isotope, whether as a consequence of missing the variation in the low k_y region, the correct offset from the gyroBohm result, or a combination of the two.

To summarise the findings of this section, then in order for quasilinear models to capture the isotope scaling of turbulent fluxes seen in nonlinear gyrokinetics, one must have a saturation rule that accurately predicts the spectral shape of the potentials around the peak, as well as captures the α_A line characteristics observed in figure 5(b). The model must therefore have sufficient functional complexity to capture the variation of the scaling with k_y in the low k_y region, and an accurate prediction of the offset. A new saturation rule, derived in light of these observations, will now be considered.

5 New saturation rule

This section details the construction of the new saturation rule SAT3, which will for the first time recreate the properties of the isotope scaling seen in the previous section. A summary of the model is presented in Section 5.7.

In the calculation of quasilinear fluxes, saturation rules are only strictly required to predict the 1D grid-independent saturated potentials, $\left\langle \left| \delta\hat{\phi}_{k_y} \right|^2 \right\rangle_{x,\theta,t} / \Delta k_y$, however in the interest of generality the two dimensional spectrum in k_y and k_x will first be considered, $\left\langle \left| \delta\hat{\phi}_{k_x,k_y} \right|^2 \right\rangle_{\theta,t}$. One can obtain the 1D potentials needed from the 2D spectrum simply

by summing the potentials over k_x, as in equation 5.

5.1 2D spectrum

For all cases in the database observed and at all values of k_y, some common features exist regarding the 2D potential slices in k_x, a representative example of which is shown in figure 6. All spectra considered are approximately even functions about a single peaked value, and tend to 0 for large $|k_x|$. Due to the absence of any symmetry-breaking effects [47] in the database, the spectra are always observed to peak at $k_x = 0$. It has been shown however that in at least the case of non-zero $E \times B$ shear a shift in the peak can be produced [48–50], and so a non-zero peak position $K(k_y)$ is considered in the following.
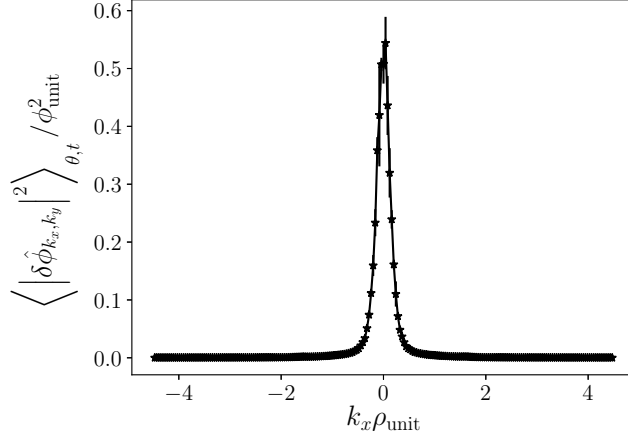
Figure 6: Example of a k_x-slice of the 2D potential magnitude spectrum, exhibiting the common features of an even, singularly peaked function with vanishing limits. Taken from the GA-std case in D, for $k_y \rho_{\text{unit}} = 10/39 = 0.256$.

The foregoing observations can all be accommodated into a functional description of the spectra by Taylor expanding the inverse of the potentials with the form

$$\frac{1}{\left\langle \left| \delta \hat{\phi}_{k_x,k_y} \right|^2 \right\rangle_{\theta,t}} = C_0\left(k_y\right) + \left(k_x - K\left(k_y\right)\right)^2 C_1\left(k_y\right) + \left(k_x - K\left(k_y\right)\right)^4 C_2\left(k_y\right) + ... \tag{10}$$

where $C_i(k_y)$ are k_y-dependent Taylor coefficients yet to be determined. Evaluating equation 10 at $k_x = K$, one finds $C_0(k_y) = 1/\left\langle \left| \delta \hat{\phi}_{k_x=K,k_y} \right|^2 \right\rangle_{\theta,t}$, the inverse of the potentials at the peak. By truncating the expansion at $\mathcal{O}(k_x^4)$, taking out a factor of C_0, relabelling the coefficients $C_i/C_0 \to C_i$ and inverting the equation one obtains

$$\left\langle \left| \delta \hat{\phi}_{k_x,k_y} \right|^2 \right\rangle_{\theta,t} = \frac{\left\langle \left| \delta \hat{\phi}_{k_x=K,k_y} \right|^2 \right\rangle_{\theta,t}}{1 + C_1\left(k_y\right)\left(k_x - K\left(k_y\right)\right)^2 + C_2\left(k_y\right)\left(k_x - K\left(k_y\right)\right)^4}. \tag{11}$$

The physical interpretation of the coefficients C_1, C_2 and K can be determined from considerations of the first three k_x moments of the 2D spectrum. The zeroth order moment is simply the 1D potential, given by equation 5. The first and second order moments define the mean value of k_x ($\langle k_x \rangle$) and the radial width of the spectrum $\left(\sigma_{k_y} = \sqrt{\langle k_x^2 \rangle - \langle k_x \rangle^2} \right)$ respectively,

$$\langle k_x \rangle = \frac{\sum_{k_x} k_x \left\langle \left| \delta \hat{\phi}_{k_x,k_y} \right|^2 \right\rangle_{\theta,t}}{\left\langle \left| \delta \hat{\phi}_{k_y} \right|^2 \right\rangle_{x,\theta,t}} \tag{12}$$

10

$$\sigma_{k_y}^2 = \frac{\sum_{k_x} (k_x - \langle k_x \rangle)^2 \left\langle \left| \delta \hat{\phi}_{k_x,k_y} \right|^2 \right\rangle_{\theta,t}}{\left\langle \left| \delta \hat{\phi}_{k_y} \right|^2 \right\rangle_{x,\theta,t}}. \tag{13}$$

By approximating the summations over k_x in equations 5, 12 and 13 as integrals via $\sum_{x=a}^{b} f(x_i) \Delta x \approx \int_a^b f(x)\,\mathrm{d}x$ and using the expression given by equation 11 for the 2D potential spectrum, one can evaluate the resulting integrals over k_x analytically (Appendix E). Assuming a sufficiently small Δk_x and a sufficiently large limit, one can show

$$K = \langle k_x \rangle, \qquad C_2(k_y) = \frac{1}{\sigma_{k_y}^4}, \qquad C_1(k_y) = \left[\left(\frac{\pi \left\langle \left| \delta \hat{\phi}_{k_x = \langle k_x \rangle, k_y} \right|^2 \right\rangle_{\theta,t} \sigma_{k_y}}{\Delta k_x \left\langle \left| \delta \hat{\phi}_{k_y} \right|^2 \right\rangle_{x,\theta,t}} \right)^2 - 2 \right] \frac{1}{\sigma_{k_y}^2} \tag{14}$$

and thus equation 11 becomes

$$\left\langle \left| \delta \hat{\phi}_{k_x,k_y} \right|^2 \right\rangle_{\theta,t} = \frac{\left\langle \left| \delta \hat{\phi}_{k_x = \langle k_x \rangle, k_y} \right|^2 \right\rangle_{\theta,t}}{1 + \left[\left(\frac{\pi \left\langle \left| \delta \hat{\phi}_{k_x = \langle k_x \rangle, k_y} \right|^2 \right\rangle_{\theta,t} \sigma_{k_y}}{\Delta k_x \left\langle \left| \delta \hat{\phi}_{k_y} \right|^2 \right\rangle_{x,\theta,t}} \right)^2 - 2 \right] \left(\frac{k_x - \langle k_x \rangle}{\sigma_{k_y}} \right)^2 + \left(\frac{k_x - \langle k_x \rangle}{\sigma_{k_y}} \right)^4}. \tag{15}$$

The prefactor of the k_x^2 term can be interpreted in relation to the normalised fall-off from the spectrum peak. Evaluating equation 15 at $k_x = \langle k_x \rangle \pm \sigma_{k_y}$, one finds:

$$\left(\frac{\pi \left\langle \left| \delta \hat{\phi}_{k_x = \langle k_x \rangle, k_y} \right|^2 \right\rangle_{\theta,t} \sigma_{k_y}}{\Delta k_x \left\langle \left| \delta \hat{\phi}_{k_y} \right|^2 \right\rangle_{x,\theta,t}} \right)^2 = \frac{\left\langle \left| \delta \hat{\phi}_{k_x = \langle k_x \rangle, k_y} \right|^2 \right\rangle_{\theta,t}}{\left\langle \left| \delta \hat{\phi}_{k_x = \langle k_x \rangle \pm \sigma_{k_y}, k_y} \right|^2 \right\rangle_{\theta,t}}. \tag{16}$$

Equation 15 is similar to that used in TGLF's SAT1 and SAT2 [1, 31], in which the potentials are modelled as a squared Lorentzian, which assumes $\sigma_{k_y}^2 C_1(k_y) = 2$ for all k_y in all cases[3]. Equation 15 generalises this assumption, retaining a degree of freedom in the description of the fall-off of the spectrum. The measured NL CGYRO values of $\sqrt{\sigma_{k_y}^2 C_1(k_y)}$ for the GA-standard case in D are shown in figure 7(a) exhibiting strong variation against k_y, particularly in the low k_y region, indicating the value of this generalisation.

The quality of adherence to the data for equation 15 is demonstrated in figures 7(b) and 7(c), using the radially-extended GA-std D simulation. Calculating the moments from the raw data, it can be observed that the functional form holds extremely well over a wide domain and many orders of magnitude in range. To explore the different cascade regimes predicted by this equation, the simplifying notation here is introduced such that equation 15 is written:

$$P(X) = \frac{P_0}{1 + CX^2 + X^4} \tag{17}$$

where $P = \left\langle \left| \delta \hat{\phi}_{k_x,k_y} \right|^2 \right\rangle_{\theta,t}$, $X = \left| (k_x - \langle k_x \rangle)/\sigma_{k_y} \right|$, $P_0 = \left\langle \left| \delta \hat{\phi}_{k_x = \langle k_x \rangle, k_y} \right|^2 \right\rangle_{\theta,t}$ and $C = \sigma_{k_y}^2 C_1(k_y)$. Assuming $\sqrt{C} \gg 1$, three distinct regions of scaling are predicted[4]:

$$P \approx \begin{cases} P_0 & X \ll \frac{1}{\sqrt{C}} \\ \frac{P_0}{CX^2} & \frac{1}{\sqrt{C}} \ll X \ll \sqrt{C} \\ \frac{P_0}{X^4} & X \gg \sqrt{C} \end{cases} \tag{18}$$

which are seen to be present in the data, as evidenced by the model-data agreement between the limiting regions marked in 7(c).

---

[3]The values of σ_{k_y} for SAT1 and SAT2 are obtained via best-fit close to the peak of the data rather than calculation, and so can be considered an 'effective width' if the spectrum *were* a squared Lorentzian.

[4]As one reduces the value of $\sqrt{C}$ to ~ 1, and further to $\sqrt{C} \ll 1$, the P_0/CX^2 scaling is found to be suppressed.
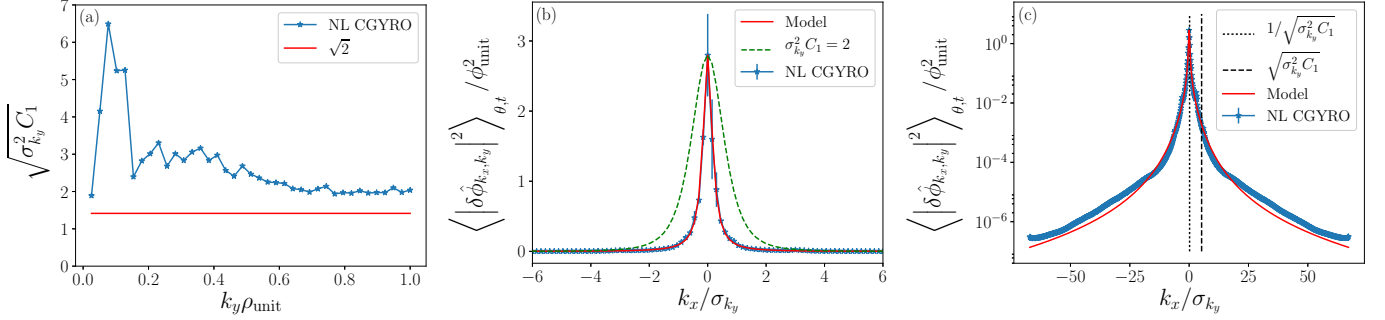
Figure 7: (a) Measured values of $\sqrt{\sigma_{k_y}^2 C_1}$ against $k_y \rho_{\text{unit}}$ for the radially-extended ($N_x = 896$) GA-standard case simulation in D, with $\sqrt{\sigma_{k_y}^2 C_1} = \sqrt{2}$ marked in red, corresponding to the squared Lorentzian assumption. (b) An example of equation 15 (red) applied to NL CGYRO data (blue) for $k_y \rho_{\text{unit}} = 5/39 = 0.128$ of the radially-extended GA-std case, plotted against k_x / σ_{k_y}. The squared Lorentzian model with the spectral width taken from the raw data is shown in green. (c) The same spectrum as (b) shown on a logarithmic y-axis, with the predicted scaling regime limits marked.

Having modelled the k_x-dependence for the spectrum, the k_y-dependence will now be considered. Four as-yet unmodelled k_y-dependent quantities are present in equation 15: The 1D potential $\left\langle \left| \delta\hat{\phi}_{k_y} \right|^2 \right\rangle_{x,\theta,t}$, the spectrum peak $\left\langle \left| \delta\hat{\phi}_{k_x = \langle k_x \rangle, k_y} \right|^2 \right\rangle_{\theta,t}$, the peak position $\langle k_x \rangle$ and the radial spectral width σ_{k_y}. In order to have a full 2D potential model, one must uniquely constrain these quantities by providing four equations describing them. This is the chosen method of TGLF SAT1 [31], for which one of the four equations is the squared Lorentzian assumption. However, flux calculations ultimately only use the 1D potential, $\left\langle \left| \delta\hat{\phi}_{k_y} \right|^2 \right\rangle_{x,\theta,t}$, and so technically this is the only quantity that needs to be prescribed for a reduced model. This potential could be modelled directly as a 1D function of k_y, such as is done by QuaLiKiz [51], but attempting to relate the remaining spectral quantities to one another first can help to establish a more firm physics basis.

5.2 Saturation equations

5.2.1 Radial spectral width parameterisation

The following relation was discovered predominantly via empirical experimentation with the database, and describes a seemingly fundamental relation between the zeroth radial moment and the second order radial moment of the 2D spectrum. It is observed that the zeroth moment is very well modelled by the equation

$$\frac{\left\langle \left| \delta\hat{\phi}_{k_y} \right|^2 \right\rangle_{x,\theta,t}}{\Delta k_y} = c_0 \sigma_{k_y}^{c_1} \tag{19}$$

for $k_y > 0$, where c_0 and c_1 are case-dependent parameters. When allowing these parameters to be fitted to the NL CGYRO data, as shown for various cases in figure 8, it can be seen that the two curves adhere to one another extremely closely[5]. Per case, this constitutes only two fitted parameters for 39 data points, rendering there no question of over-fitting. Moreover, the measured value of the exponent c_1 is found to be strongly consistent across cases, as displayed in figure 9, with an approximate value of $c_1 = -2.42$ for the database.

This observation is perhaps the most important point of this work, as it appears to describe a general and robust relation between two hypothetically-independent moments of the 2D potential spectrum. Somewhat counter-intuitively it suggests that the area under the radial spectrum, related to the zeroth moment, is independent of its peak value,

---

[5]For reference, example data for $\sigma_{k_y} \rho_{\text{unit}}$ corresponding to the case of figure 8(a) is shown in figure 10.
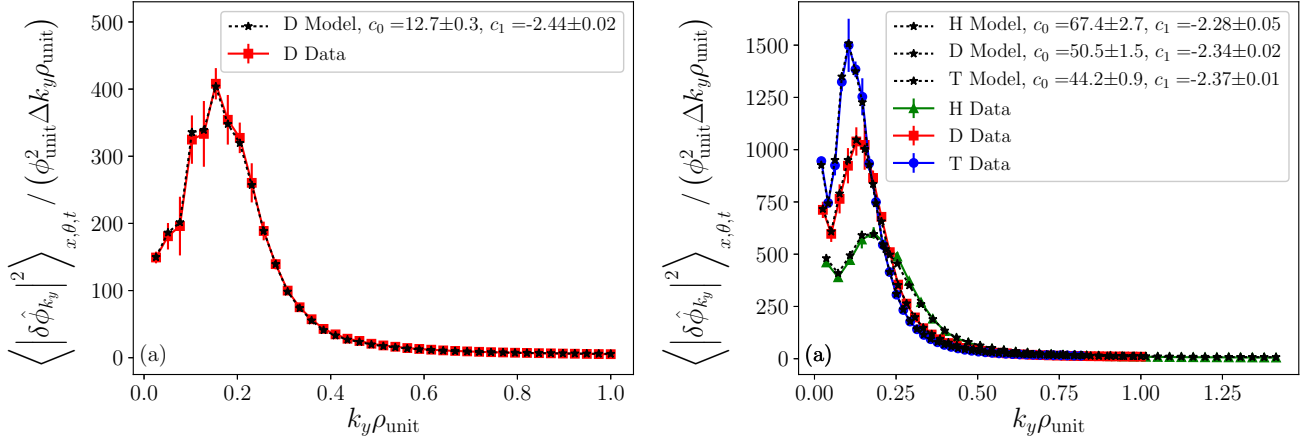
Figure 8: (a) The model of equation 19 (black) applied to the NL CGYRO grid-independent potentials of the GA-standard case in D (red), allowing the two parameters to be fitted to the data. (b) Further examples of equation 19, for the $a/L_n = 3.0$, $\nu_{ee}(a/c_s) = 0.01$ case in H, D and T.

and instead only depends on the width. This observed relation is understood to be novel, and a physical mechanism for why this is the case is yet to be put forward. It is this observation that forms the core of the new saturation rule.
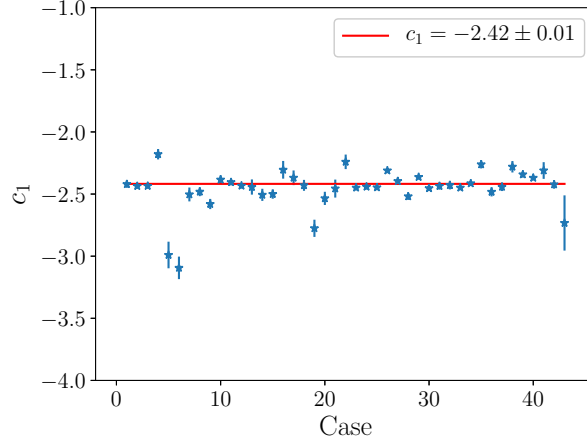

Figure 9: Measured values of the c_1 parameter across all nonlinear simulations in the database. The error bars shown are the uncertainties in the fitted parameter c_1.

5.2.2 Parameter considerations

Given sufficient ability to model the case-dependent values of c_0 and c_1, equation 19 provides one of the four equations necessary to uniquely define the 2D potential spectrum. However, for every parameter introduced by such equations, a linear-physics based model for its case-dependent calculation will be required. Because equation 19 implies that the 1D potential is independent of the peak spectrum value and $\langle k_x \rangle$, the choice is made in this work to model σ_{k_y} only. Doing so will leave the 2D spectrum with an arbitrary peak value and location, but will have both its zeroth and second moments defined.

5.2.3 Model for the radial spectral width

To inform the model for σ_{k_y}, a representative plot is shown in figure 10. Equation 19 implies two important qualities of σ_{k_y}: firstly, that the characteristic peak observed in the 1D potentials should correspond to a minimum in σ_{k_y} at

the same position in k_y, which is indeed seen, and is denoted $k_{\min}$. This is the first time this observation has been made, in part due to the well-resolved fluctuation averages obtained from extended simulation times and the increased density of binormal grid-points used in the database. The second quality is that, because the values of the potentials away from the peak are comparatively small and contribute negligibly to the overall flux, the accurate modelling of σ_{k_y} in this higher k_y region is less fundamental to successful flux prediction.
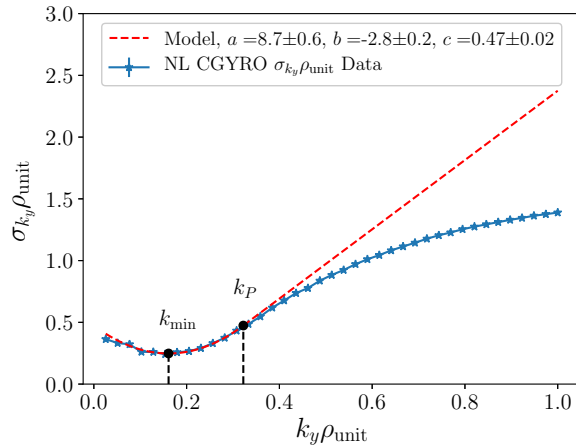

Figure 10: Example of $\sigma_{k_y}\rho_{\mathrm{unit}}$ data obtained for the GA-standard case in D (blue). In red is the model for the widths given by equation 20, with the parameters a, b and c fitted to the data. Also marked are $k_{\min}$ and k_P, the positions of the minimum and piecewise connection point respectively.

To incorporate the observed minimum into the model a quadratic polynomial is used. A quadratic over the entire k_y domain capturing this minimum can however become too large in the middle k_y region, and so a piecewise function is constructed, with a first-order polynomial used past a certain point, k_P. This is taken to be $k_P = 2k_{\min}$. The two regions are connected by imposing continuity of the function, as well as continuity of the gradient, at $k_y = k_P$:

$$\sigma_{k_y} = \begin{cases} ak_y^2 + bk_y + c & 0 < k_y \leq k_P \\ \left(2ak_P + b\right)k_y + c - ak_P^2 & k_P < k_y \leq \infty \end{cases} \tag{20}$$

where a, b and c are coefficients to be modelled. Here the function is assumed to extend to infinity.

By combining equations 19 and 20, one obtains an equation for the 1D potentials solely as a function of k_y and the parameters $\{c_0, c_1, a, b, c\}$. To make progress in modelling these parameters, they shall first be defined in terms of more physically meaningful quantities.

5.3 Recasting the coefficients

The exponent c_1 is dimensionless and has already been fitted to the nonlinear database in figure 9, and so does not need to be recast. An expression for c_0 can be obtained by evaluating equation 19 at some given point k_0, to be determined:

$$c_0 = \frac{\left\langle \left| \delta\hat{\phi}_{k_y=k_0} \right|^2 \right\rangle_{x,\theta,t}}{\Delta k_y} \left(\frac{1}{\sigma_{k_y=k_0}} \right)^{c_1} \tag{21}$$

giving the overall saturation model as

$$\frac{\left\langle \left| \delta\hat{\phi}_{k_y} \right|^2 \right\rangle_{x,\theta,t}}{\Delta k_y} = \frac{\left\langle \left| \delta\hat{\phi}_{k_y=k_0} \right|^2 \right\rangle_{x,\theta,t}}{\Delta k_y} \left(\frac{\sigma_{k_y}}{\sigma_{k_y=k_0}} \right)^{c_1} \tag{22}$$

Equation 22 expresses the 1D potentials as a product of their magnitude at a given point k_0, $\left\langle \left| \delta\hat{\phi}_{k_y=k_0} \right|^2 \right\rangle_{x,\theta,t} / \Delta k_y$ and a k_y-dependent function describing the shape of the spectrum, $\left(\sigma_{k_y}/\sigma_{k_y=k_0} \right)^{c_1}$. These quantities are denoted the

saturation level and the spectral shape respectively. The variation with k_y observed in the potential α_A plot (figure 5(b)) comes entirely from the spectral shape, with the offset mainly attributed to the saturation level.

As the spectral widths appear only in the above normalised form for the saturation model, a reduction in the degrees of freedom is provided. Assuming $0 < k_0 \leq k_P$, one can divide through by one of the expansion coefficients in the spectral widths, chosen here to be b:

$$\frac{\sigma_{k_y}}{\sigma_{k_y=k_0}} = \begin{cases} \left(\frac{a}{b}k_y^2 + k_y + \frac{c}{b}\right) / \left(\frac{a}{b}k_0^2 + k_0 + \frac{c}{b}\right) & 0 < k_y \leq k_P \\ \left(\left(2\frac{a}{b}k_P + 1\right)k_y + \frac{c}{b} - \frac{a}{b}k_P^2\right) / \left(\frac{a}{b}k_0^2 + k_0 + \frac{c}{b}\right) & k_P < k_y \leq \infty \end{cases} \tag{23}$$

and so the number of unknown coefficients reduces from 3 to 2, now requiring only the ratios a/b and c/b. A more transparent physical interpretation of a/b can be obtained by considering the definition of the minimum of the spectral widths. Imposing a minimum at $k_{\min}$ in equation 20, one finds

$$\left.\frac{\mathrm{d}\sigma_{k_y}}{\mathrm{d}k_y}\right|_{k_y=k_{\min}} = 2ak_{\min} + b = 0 \tag{24}$$

and therefore $a/b = -1/(2k_{\min})$. With the coefficients now recast, this leaves 3 quantities to be modelled, for a given choice of k_0: $k_{\min}, c/b$, and $\left\langle\left|\delta\hat{\phi}_{k_y=k_0}\right|^2\right\rangle_{x,\theta,t}/\Delta k_y$.

Note, as of yet no appeals to linear physics have been made, the model derived thus far has come solely from considerations of nonlinear gyrokinetic spectra. By taking this bottom-up approach, the validity of the underlying functional forms of the saturation rule equations is guaranteed, up to the hypothetical quality observed when the parameters are fitted to the data. This foundation implies that as linear physics based approximations for c_1 and the three quantities above improve, the model will tend towards being as accurate as when fitted in this way.

5.4 Approximating the parameters from linear physics quantities

For TGLF's saturation rules SAT1 and SAT2, both of which are based on the saturation mechanism of zonal mixing, it is argued that the linear growth of the present plasma instabilities γ_{k_y} is damped by the competing influence of the zonal flow mixing $k_y V_{\mathrm{ZF}}$, where V_{ZF} is the zonal flow velocity. The wavenumber at which the drive-to-damping ratio of these two processes is maximised therefore provides an estimate of the location of the peak of the turbulent transport, as well as a characteristic length scale of the nonlinear saturation from the linear system. This wavenumber is denoted $k_{\max}$, and is defined by

$$\left.\frac{\mathrm{d}}{\mathrm{d}k_y}\left(\frac{\gamma_{k_y}}{k_y}\right)\right|_{k_y=k_{\max}} = 0 \tag{25}$$

with the corresponding growth rate $\gamma_{\max}$ providing an estimate of the characteristic time scale of the saturation

$$\gamma_{\max} = \gamma_{k_y=k_{\max}}. \tag{26}$$

A graphical example of the determination of these quantities for a given equilibrium is shown in figure 11.

The new saturation rule parameters $k_{\min}, c/b$, and $\left\langle\left|\delta\hat{\phi}_{k_y=k_0}\right|^2\right\rangle_{x,\theta,t}/\Delta k_y$ will now be modelled entirely from linear physics, by assuming proportionality to the dimensionally-consistent combination of the characteristic linear quantities $\gamma_{\max}$ and $k_{\max}$, as well as the equilibrium quantity B_{unit}.

Considering first the dimensionality of b and c individually from equation 20, one finds b to be dimensionless and c to have dimensions of k_y, giving c/b dimensions of k_y. The quantity $k_{\min}$ also has dimensions of k_y, and so per the method above these are both modelled as proportional to $k_{\max}$. The database-fitting exercise is carried out in figure 12, resulting in $c/b = -0.751k_{\max}$, $k_{\min} = 0.685k_{\max}$.

For the saturation level $\left\langle\left|\delta\hat{\phi}_{k_y=k_0}\right|^2\right\rangle_{x,\theta,t}/\Delta k_y$, the value of k_0 is chosen to be $k_0 = 0.6k_{\min}$, as it is at this position that the model scatter for the following is found to be minimised. The dimensionally-consistent combination of linear quantities for the saturation level is $\propto B_{\mathrm{unit}}^2\gamma_{\max}^2/k_{\max}^5$. Note that this is a similar form to that derived from considerations of balance between linear growth and turbulent $E \times B$ advection [52].
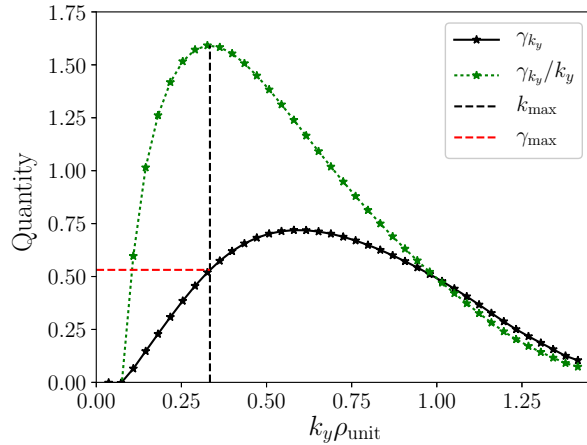
Figure 11: Demonstration of the calculation of $k_{\max}$ and $\gamma_{\max}$ from a linear growth rate spectrum, here for the $a/L_n = 3.0$ case in H. Starting from γ_{k_y} (solid black), one divides this spectrum by k_y to obtain γ_{k_y}/k_y (dashed green). The maximum of this curve is then found via quadratic interpolation, with the k_y value at which this occurs being defined as $k_{\max}$. Returning then to γ_{k_y}, the value of this curve at $k_{\max}$ is defined as $\gamma_{\max}$.
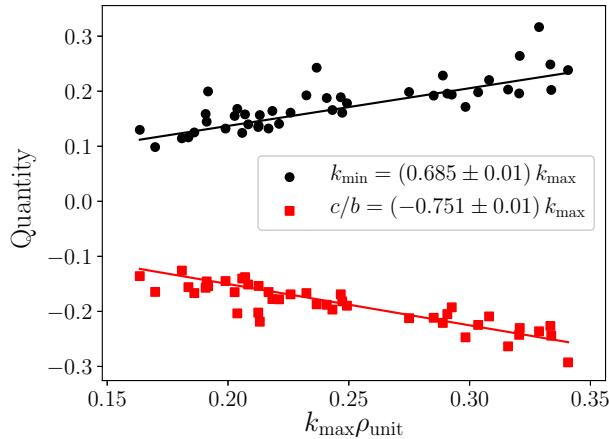

Figure 12: Fitting exercise of the two quantities modelled as proportional to $k_{\max}$ across the NL CGYRO database: $k_{\min}$ (black circles), and c/b (red squares), used in defining the model for the spectral shape $\sigma_{k_y}/\sigma_{k_y=k_0}$ (equation 23).

When tested against the database, $B_{\mathrm{unit}}^2 \gamma_{\max}^2/k_{\max}^5$ is found to be a good model for the cases in which the dominant mode is the ITG (figure 13(a)). However, for those with TEMs present, $B_{\mathrm{unit}}^2 \gamma_{\max}^2/k_{\max}^4$ in dimensionless units is found to be in much better agreement, indicating a difference in physical saturation between the two mode types (figure 13(b)). The TEM saturation in dimensional units is therefore assumed proportional to $\gamma_{\max}^2 \rho_{\mathrm{unit}} B_{\mathrm{unit}}^2/k_{\max}^4$. It is here explicitly that a large cause of the difference in isotope scaling between the two mode types can be seen, and the reason why previous saturation models have failed to recreate the isotope scalings seen in TEM-dominated turbulence.

To explain why this factor of $k_{\max}\rho_{\mathrm{unit}}$ affects the isotope scaling, consider first this quantity in a system with adiabatic electrons. In such a situation, all quantities are exactly gyroBohm scaled, such that for three linear simulations in H, D and T the value of $k_{\max}$ occurs at the same value of $k_y\rho_i$. Because $\rho_i \propto \sqrt{A}$, one finds in the adiabatic electron case that $k_{\max} \propto A^{-0.5}$. In the simulations of this work, for which kinetic electrons have been used, the scaling of $k_{\max}$ with A generally becomes slightly more positive at around $\alpha_A \approx -0.3$, which is sufficient to capture the differences between the isotope scalings of the two mode types' saturation levels.

The above kinetic electron physics will be captured in the saturation model by using two different saturation levels for the ITG and TEM, such that one has $12.7 B_{\mathrm{unit}}^2 \gamma_{\max}^2 \rho_{\mathrm{unit}}/k_{\max}^4$ for the TEM, and $3.3 B_{\mathrm{unit}}^2 \gamma_{\max}^2/k_{\max}^5$ for the ITG, where the proportionality constants are taken from figure 13. In order to decide which saturation level to
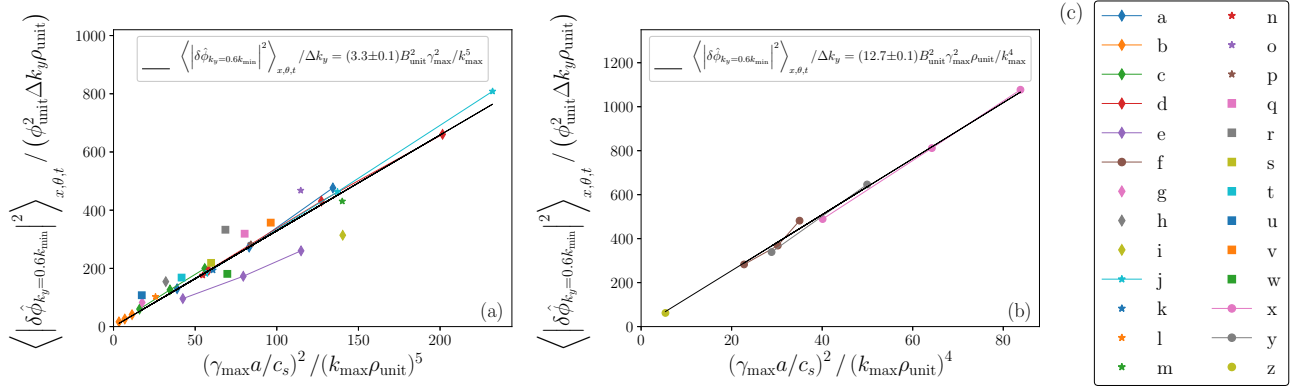
Figure 13: Potential magnitudes evaluated at $0.6k_{\mathrm{min}}$ against a combination of linear quantities ((a) and (b)). Subfigure (c) displays the marker type used for each case, with the labels corresponding to those shown in table 1. Data points of the same colour connected by a line indicate simulations of the same equilibrium but of different isotopes. In (a), the cases with a dominant ITG instability scale approximately with $B_{\mathrm{unit}}^2 \gamma_{\mathrm{max}}^2/k_{\mathrm{max}}^5$, however for those that are TEM-dominated (cases f, x, y and z, shown in (b)), a scaling of $B_{\mathrm{unit}}^2 \gamma_{\mathrm{max}}^2 \rho_{\mathrm{unit}}/k_{\mathrm{max}}^4$ is found to be in much better agreement, indicating a difference in saturation level between the two mode types.

use for a given simulation, the linear physics must be considered to reveal whether the turbulence is ITG- or TEM-dominated. For SAT3, the ratio between the magnitude of the linear energy weights of the electrons and ions is used, $\left|W_{e,k_y}^{\mathrm{L}}\right|/\left|W_{i,k_y}^{\mathrm{L}}\right| = \left|W_{e,k_y}^{\mathrm{L}}/W_{i,k_y}^{\mathrm{L}}\right|$, due to the disparate behaviour in the ratio of the species' energy fluxes for the two mode types [53]. For ion-dominated turbulence, in which the electron energy fluxes are comparatively small, one expects the ratio of $\left|W_{e,k_y}^{\mathrm{L}}/W_{i,k_y}^{\mathrm{L}}\right|$ to also be small. When in the regime of TEM turbulence however, the electron turbulent energy flux increases to approximately the level of the ions. The ratio of $\left|W_{e,k_y}^{\mathrm{L}}/W_{i,k_y}^{\mathrm{L}}\right|$ can be calculated from linear physics, and so represents a useful metric to select between the two saturation levels. If new classes of modes were present, this aspect of the saturation rule would likely need to be revisited and extended further.

A plot of $\left|W_{e,k_y}^{\mathrm{L}}/W_{i,k_y}^{\mathrm{L}}\right|$ for all cases in the database against k_y/k_{max} is shown in figure 14, with ITG cases in red and TEM cases in blue. It can be seen that the TEM cases cluster around a value of $\left|W_{e,k_y}^{\mathrm{L}}/W_{i,k_y}^{\mathrm{L}}\right| \approx 1$, whereas ITG cases are mainly grouped around 0.4.
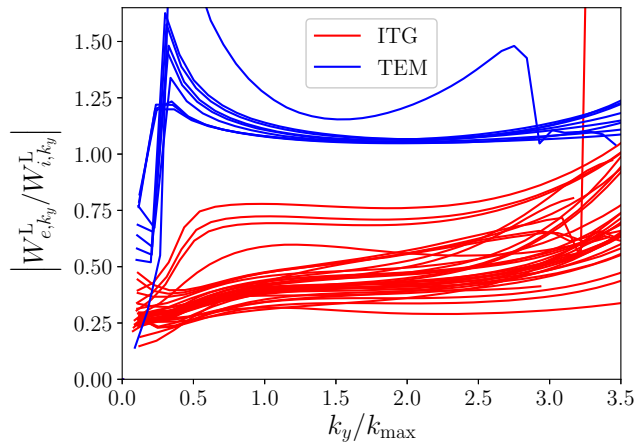

Figure 14: Ratios of the linear electron energy weight magnitudes to the linear ion energy weight magnitudes $\left|W_{e,k_y}^{\mathrm{L}}/W_{i,k_y}^{\mathrm{L}}\right|$ against k_y/k_{max} for the database. Cases for which the dominant linear instability is the TEM are in blue, and those with ITG are shown in red. Note the disparate grouping between the mode types.

A transition function is now defined for the two modes, as a function of the weight ratio evaluated at $k_y = k_{\mathrm{max}}$. At

values below $\left|W_{e,k_y}^{\mathrm{L}}/W_{i,k_y}^{\mathrm{L}}\right|_{k_y=k_{\max}} = 0.8$ the ITG scaling is used, and at values of 1 and above the TEM scaling is used, with a first-order polynomial in-between to connect the two regions. The mode transition function $M(x; x_1, x_2, y_1, y_2)$ is introduced such that

$$M(x; x_1, x_2, y_1, y_2) = \begin{cases} y_1 & x \leq x_1 \\ y_1 \frac{x_2-x}{x_2-x_1} + y_2 \frac{x-x_1}{x_2-x_1} & x_1 < x \leq x_2 \\ y_2 & x_2 < x \end{cases} \tag{27}$$

which allows the potentials evaluated at k_0 to be written

$$\frac{\left\langle \left|\delta\hat{\phi}_{k_y=k_0}\right|^2 \right\rangle_{x,\theta,t}}{\Delta k_y} = M\left(\left|\frac{W_{e,k_y}^{\mathrm{L}}}{W_{i,k_y}^{\mathrm{L}}}\right|_{k_y=k_{\max}} ; 0.8,\ 1.0,\ 3.3\frac{\gamma_{\max}^2}{k_{\max}^5},\ 12.7\frac{\gamma_{\max}^2 \rho_{\mathrm{unit}}}{k_{\max}^4}\right) B_{\mathrm{unit}}^2. \tag{28}$$

It can be shown that measuring the sign of the linear frequency at a position in k_y can also be used to differentiate between the two mode types, however the above was chosen to attempt to avoid discontinuous changes in flux at the point of a mode transition.

5.5 Model extensions

5.5.1 $E \times B$ shear

Modern quasilinear models are required to include the effects of equilibrium $E \times B$ shear, a mechanism that can both generate turbulent momentum transport, as well as suppress turbulence in other channels. This effect is incorporated through an equilibrium input parameter, the shearing rate γ_E, and the consequences of non-zero $E \times B$ shear must be explicitly defined in the saturation rule. Although no such cases were considered in the database, one can simply isolate the $E \times B$ effect of a previous rule and incorporate it into the new model. Using an apostrophe to denote said previous rule, taken in this work to be that of TGLF's SAT2 [1], one defines the effect of shear F'_{s,k_y} as the ratio of flux components with shear to those without

$$F'_{s,k_y}(\gamma_E) = \frac{Q'_{s,k_y}(\gamma_E)}{Q'_{s,k_y}(\gamma_E = 0)}. \tag{29}$$

The flux components of the new saturation rule are then obtained simply by multiplying F'_{s,k_y} by the flux components of the new rule without flow shear, $Q_{s,k_y}(\gamma_E) = F'_{s,k_y}(\gamma_E) Q_{s,k_y}(\gamma_E = 0)$. Taking the ratio of the flux components as opposed to the potentials bypasses any complications arising from differences in definitions between the two saturation rules. Looking at TGLF SAT2, one finds

$$F'_{s,k_y}(\gamma_E) = \frac{\tilde{W}_{s,k_y,k_x=k_{x0}}^{\mathrm{L}}/\tilde{W}_{s,k_y,k_x=0}^{\mathrm{L}}}{\left(1 + \left(\alpha_x \frac{k_{x0}}{k_x^{\mathrm{model}}}\right)^{\sigma_x}\right)^2 \left(1 + \left(\frac{k_{x0}}{k_x^{\mathrm{model}}}\right)^2\right)^2} \tag{30}$$

which is the function incorporated into SAT3. Here $\tilde{W}_{s,k_y,k_x}^{\mathrm{L}}$ is the quasilinear weight defined by TGLF, which is evaluated at a single k_x rather than a sum over k_x. The two constants are $\alpha_x = 1.21$ and $\sigma_x = 2$, with $k_{x0} = 0.32 k_y (k_{\max}/k_y)^{0.7} (\gamma_E/\gamma_{\max})$ and

$$k_x^{\mathrm{model}} = \begin{cases} \frac{0.76 k_{\max}}{\sqrt{g^{xx}(\theta=0)}} & k_y < 0.76 k_{\max} \\ \frac{0.76 k_{\max}}{\sqrt{g^{xx}(\theta=0)}} + \frac{1.22}{\sqrt{g^{xx}(\theta=0)}} \frac{B(\theta=0)}{B_{\mathrm{unit}}} (k_y - 0.76 k_{\max}) & k_y \geq 0.76 k_{\max} \end{cases} \tag{31}$$

where $g^{xx} = |\nabla x|^2$.

5.5.2 Mixed plasmas

For all simulations in the database of this work a pure plasma was used. For generality, quasilinear models must be able to operate with multiple ion species. The only aspect of SAT3 that is explicitly affected by this generalisation is

the ratio of the magnitude of the linear weights $\left|W^{\mathrm{L}}_{e,k_y}/W^{\mathrm{L}}_{i,k_y}\right|$, used as an argument in the mode transition function, as this becomes ambiguously defined in a plasma with multiple ion species.

This ambiguity is resolved by changing the denominator of the linear weight ratio to the sum over ion weights, $\left|W^{\mathrm{L}}_{e,k_y}/W^{\mathrm{L}}_{i,k_y}\right| \rightarrow \left|W^{\mathrm{L}}_{e,k_y}/\sum_i W^{\mathrm{L}}_{i,k_y}\right|$ for ion species i. By conducting a scan over relative concentrations of D and T in the GA-std and $a/L_n = 3.0$ cases linearly (figure 15), this new ratio is shown to be invariant with relative density and thus recreate the expected behaviour.
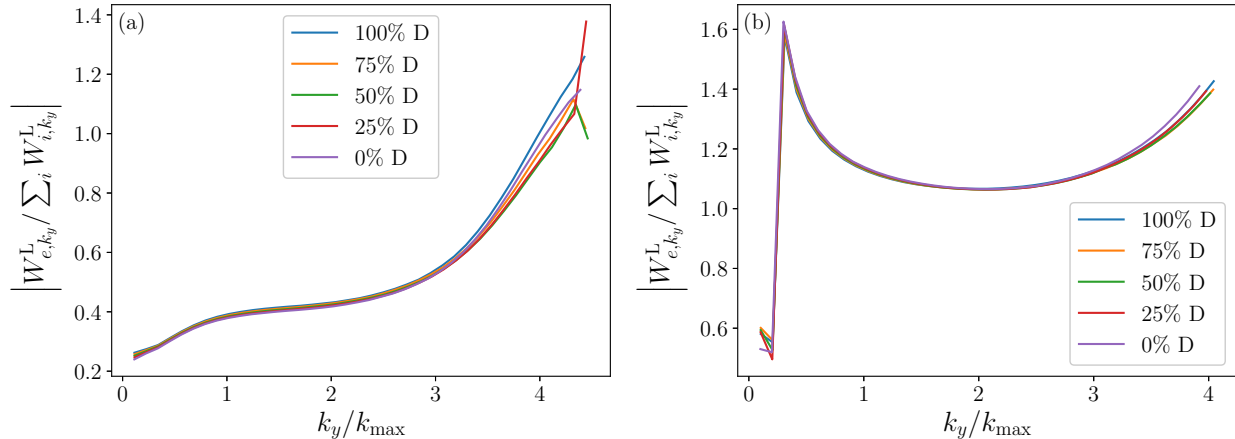

Figure 15: Linear energy weight magnitude ratios $\left|W^{\mathrm{L}}_{e,k_y}/\sum_i W^{\mathrm{L}}_{i,k_y}\right|$ for different relative concentrations of D and T against $k_y/k_{\max}$ for the GA-std case (a) and the $a/L_n = 3.0$ case (b). Note the essential invariance across the spectrum for the different concentrations.

5.6 Quasilinear approximation functions

Having described the saturated potentials, the QLA functions are now considered, defined in equation 7. In general for electrostatic turbulence there are $3n_s$ of these functions, where n_s is the total number of species present, with one existing for each combination of the 3 velocity moments and species. Historically these functions have seen a comparatively small amount of focus compared to the potentials, and are typically modelled as a constant [51]. By plotting these functions explicitly from the CGYRO data, one can determine to what degree a constant QLA is a reasonable assumption to make.

All cases in this database use kinetic electrons and a single ion species, giving 6 functions. Of these 6, the two momentum QLA functions are trivially zero, due to there being no momentum transport in the cases considered, and the two particle functions are identical, as a consequence of ambipolarity. This leaves three as non-trivial: the two energy functions for the ion and electrons, and one of the particle functions.

Plots of these three QLA functions against $k_y\rho_i$ are shown in figure 16 for all cases in the database. The vast majority of the energy functions for both species have a similar shape across the spectrum, and most importantly exhibit relatively small variation in the region where the flux components are largest ($k_y\rho_i \sim 0.2$, evidenced in figure 3(a)). A similar description is seen for the particle function, although with more sporadic variation in some cases. The assumption that the QLA could be modelled as constant was found to be a reasonable approximation for the database, with the constants for the model being set by minimising the scatter between the NL CGYRO flux data and the CGYRO-SAT3 flux data. The values of these constants for the electron and ion fluxes were found to be similar, however were stratified by mode type and moment. These are $\Lambda^{\Gamma}_{\mathrm{ITG}} = 1.1$, $\Lambda^{\Gamma}_{\mathrm{TEM}} = \Lambda^{Q}_{\mathrm{TEM}} = 0.6$ and $\Lambda^{Q}_{\mathrm{ITG}} = 0.75$. To capture these differences, the QLA functions are expressed in terms of the mode transition function (equation 27), such that for the particle flux

$$\Lambda^{\Gamma}_{s,k_y} = M\left(\left|\frac{W^{\mathrm{L}}_{e,k_y}}{\sum_i W^{\mathrm{L}}_{i,k_y}}\right|_{k_y=k_{\max}}; 0.8, 1.0, 1.1, 0.6\right) \tag{32}$$
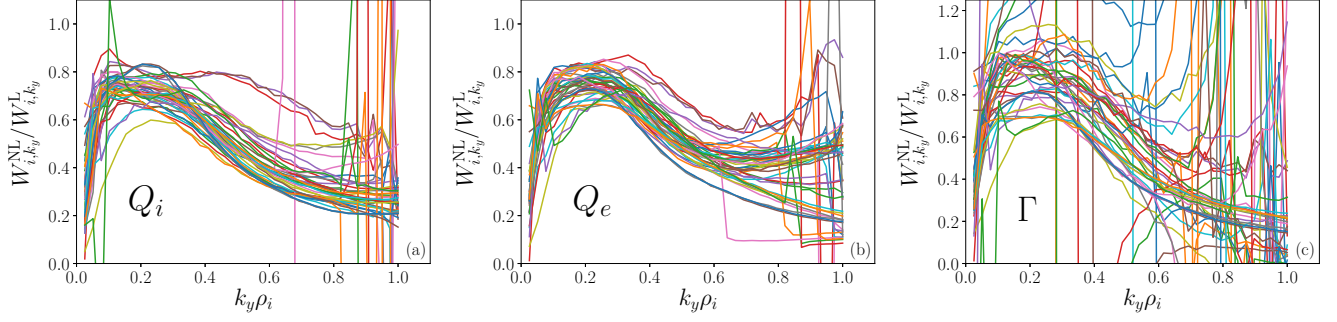
19

Figure 16: QLA functions for all cases in the database, showing those for (a) ion energy flux, (b) electron energy flux and (c) particle flux.

and for the energy flux

$$\Lambda^Q_{s,k_y} = M \left(\left| \frac{W^{\mathrm{L}}_{e,k_y}}{\sum_i W^{\mathrm{L}}_{i,k_y}} \right|_{k_y=k_{\max}} ; 0.8, 1.0, 0.75, 0.6 \right). \tag{33}$$

Any other forms of transport are assumed to have $\Lambda_{s,k_y} = 0.8$.

While a mode-dependent constant remains a reasonable model for the contribution of the QLA functions to the overall flux in this database, it is not perfect, missing for example the isotope scaling seen in figure 4. In future studies more exotic tokamak equilibria may cause the QLA functions to deviate further from those seen here, potentially necessitating an effort to try to predict their shapes from linear physics.

5.7 Summary of new saturation model, SAT3

The entirety of SAT3 is collected here for reference. The fluxes of the model are constructed via

$$Q_s = 2 \sum_{k_y>0} \Lambda_{s,k_y} W^{\mathrm{L}}_{s,k_y} F_{s,k_y} \left[\frac{\left\langle \left| \delta\hat{\phi}_{k_y} \right|^2 \right\rangle_{x,\theta,t}}{\Delta k_y} \right] \Delta k_y \tag{34}$$

where Λ_{s,k_y} is the quasilinear approximation (QLA) function, W^{L}_{s,k_y} is the linear weight for species s, F_{s,k_y} describes the effect of $E \times B$ shear, $\left\langle \left| \delta\hat{\phi}_{k_y} \right|^2 \right\rangle_{x,\theta,t} / \Delta k_y$ is the saturated potential, and Δk_y is the binormal grid spacing of the simulation. The model for the saturated potentials is

$$\frac{\left\langle \left| \delta\hat{\phi}_{k_y} \right|^2 \right\rangle_{x,\theta,t}}{\Delta k_y} = M \left(\left| \frac{W^{\mathrm{L}}_{e,k_y}}{\sum_i W^{\mathrm{L}}_{i,k_y}} \right|_{k_y=k_{\max}} ; 0.8, 1.0, 3.3\frac{\gamma^2_{\max}}{k^5_{\max}}, 12.7\frac{\gamma^2_{\max}\rho_{\mathrm{unit}}}{k^4_{\max}} \right) B^2_{\mathrm{unit}} \left(\frac{\sigma_{k_y}}{\sigma_{k_y=k_0}} \right)^{-2.42} \tag{35}$$

where M is the mode transition function

$$M(x; x_1, x_2, y_1, y_2) = \begin{cases} y_1 & x \leq x_1 \\ y_1 \frac{x_2-x}{x_2-x_1} + y_2 \frac{x-x_1}{x_2-x_1} & x_1 < x \leq x_2 \\ y_2 & x_2 < x \end{cases} \tag{36}$$

which captures the disparate saturation levels between ITG- and TEM-dominated turbulence. The wavenumber $k_{\max}$ is defined as the position of the maximum of the linear growth rate divided by k_y,

$$\frac{\mathrm{d}}{\mathrm{d}k_y}\left(\frac{\gamma_{k_y}}{k_y}\right)\Bigg|_{k_y=k_{\max}} = 0 \tag{37}$$

and $\gamma_{\max} = \gamma_{k_y=k_{\max}}$. The reference magnetic field B_{unit} is given by equation 3, with $\rho_{\text{unit}} = \sqrt{m_D T_e}/eB_{\text{unit}}$, and

$$\frac{\sigma_{k_y}}{\sigma_{k_y=k_0}} = \begin{cases} \left(-\frac{1}{2k_{\min}}k_y^2 + k_y + \frac{c}{b}\right) / \left(-\frac{1}{2k_{\min}}k_0^2 + k_0 + \frac{c}{b}\right) & 0 < k_y \le k_P \\ \left(\left(-\frac{1}{k_{\min}}k_P + 1\right)k_y + \frac{c}{b} + \frac{1}{2k_{\min}}k_P^2\right) / \left(-\frac{1}{2k_{\min}}k_0^2 + k_y + \frac{c}{b}\right) & k_P < k_y \le \infty \end{cases} \tag{38}$$

where $c/b = -0.751k_{\max}$, $k_{\min} = 0.685k_{\max}$, $k_0 = 0.6k_{\min}$ and $k_P = 2k_{\min}$.

The quasilinear approximation functions Λ_{s,k_y} vary depending on velocity moment and mode type. For the particle flux and energy flux these are

$$\Lambda_{s,k_y}^{\Gamma} = M\left(\left|\frac{W_{e,k_y}^{\text{L}}}{\sum_i W_{i,k_y}^{\text{L}}}\right|_{k_y=k_{\max}} ; 0.8, 1.0, 1.1, 0.6\right) \tag{39}$$

$$\Lambda_{s,k_y}^{Q} = M\left(\left|\frac{W_{e,k_y}^{\text{L}}}{\sum_i W_{i,k_y}^{\text{L}}}\right|_{k_y=k_{\max}} ; 0.8, 1.0, 0.75, 0.6\right) \tag{40}$$

with other fluxes taking $\Lambda_{s,k_y} = 0.8$.

Finally, the function F_{s,k_y} describes the effect of $E \times B$ shear and is given by [1]

$$F_{s,k_y}(\gamma_E) = \frac{\tilde{W}_{s,k_y,k_x=k_{x0}}^{\text{L}} / \tilde{W}_{s,k_y,k_x=0}^{\text{L}}}{\left(1 + \left(\alpha_x \frac{k_{x0}}{k_x^{\text{model}}}\right)^{\sigma_x}\right)^2 \left(1 + \left(\frac{k_{x0}}{k_x^{\text{model}}}\right)^2\right)^2} \tag{41}$$

where $\tilde{W}_{s,k_y,k_x}^{\text{L}}$ is the quasilinear weight defined by TGLF, which is evaluated at a single k_x rather than a sum over k_x. The two constants are $\alpha_x = 1.21$ and $\sigma_x = 2$, with $k_{x0} = 0.32k_y\left(k_{\max}/k_y\right)^{0.7}\left(\gamma_E/\gamma_{\max}\right)$ and

$$k_x^{\text{model}} = \begin{cases} \frac{0.76k_{\max}}{\sqrt{g^{xx}(\theta=0)}} & k_y < 0.76k_{\max} \\ \frac{0.76k_{\max}}{\sqrt{g^{xx}(\theta=0)}} + \frac{1.22}{\sqrt{g^{xx}(\theta=0)}}\frac{B(\theta=0)}{B_{\text{unit}}}\left(k_y - 0.76k_{\max}\right) & k_y \ge 0.76k_{\max} \end{cases} \tag{42}$$

where $g^{xx} = |\nabla x|^2$ and B is the equilibrium magnetic field magnitude.

6   Results

The scatter plots of the fluxes obtained from NL CGYRO against the results of CGYRO-SAT3 are shown in figure 17 for the ion energy fluxes, electron energy fluxes and particle fluxes. TEM-dominated cases are marked by circles (labelled f, x, y and z in figure 13(c)), with the remainder being ITG-dominated. Data points connected by a line denote simulations of the same equilibrium but different of isotopes. A metric for the quality of the model agreement can be calculated by taking the average percentage error,

$$\Sigma_Q = \frac{1}{N}\sum_{m=1}^{N}\left|\frac{Q_{\text{model},m} - Q_{\text{NL},m}}{Q_{\text{NL},m}}\right| \tag{43}$$

$$\Sigma_\Gamma = \frac{1}{N}\sum_{m=1}^{N}\left|\frac{\Gamma_{\text{model},m} - \Gamma_{\text{NL},m}}{\Gamma_{\text{NL},m}}\right| \tag{44}$$

for the energy flux and particle flux, where N is the number of simulations in the database. The values obtained for the three plots are displayed in their respective subfigures.

For comparison, the equivalent scatter plots for a rescaled CGYRO-SAT1 model are shown in figure 18, with additional fitted prefactors for each flux type, labelled CGYRO-SAT1*[6]. Looking at figures 17 and 18 a reduction in

---

[6]This accounts for the larger NL CGYRO fluxes compared to those of SAT1's training database, which resulted from an increased binormal resolution in this work. These pre-factors were fitted to the D simulations of the ITG-dominated cases, and are displayed in the legends of figure 18. Note that the isotope scaling of the fluxes is unaffected by a database-wide rescaling constant.

the average percentage error between CGYRO-SAT1* and CGYRO-SAT3 is seen for the three flux types. CGYRO-SAT1* and CGYRO-SAT3 can be seen to perform similarly in the ITG-dominated cases, as may be expected, however great improvement is shown in the isotope scaling and magnitude of the TEM cases, owing to the modelling of the difference in saturation level between the two mode types present in SAT3. This is demonstrated explicitly in figure 19, which exhibits the ion and electron energy fluxes against isotope mass for the ITG-dominated GA-std case and the TEM-dominated $a/L_n = 3.0$ case compared between the three models.
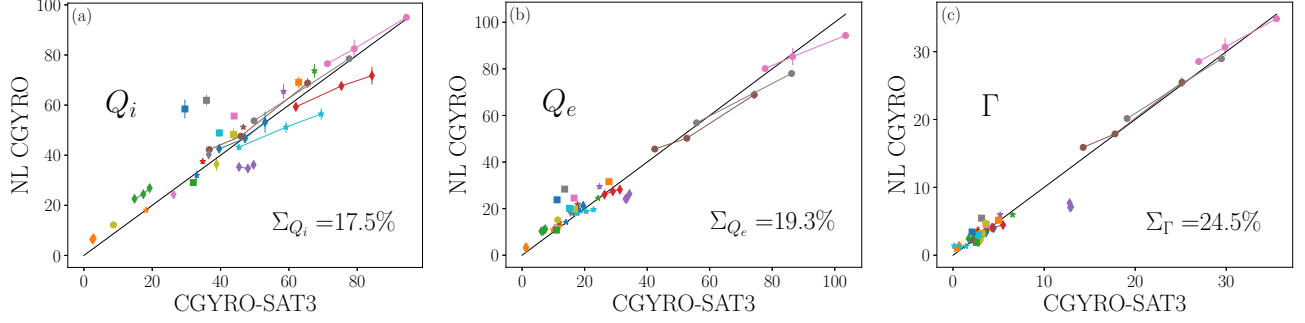

Figure 17: Scatter plots of NL CGYRO against CGYRO-SAT3 results for (a) ion energy flux, (b) electron energy flux and (c) particle flux. The legend for these figures is shown in figure 13(c). The line to denote perfect agreement between the models is shown in black, with the respective relative errors also shown on each plot, defined by equations 43 and 44.
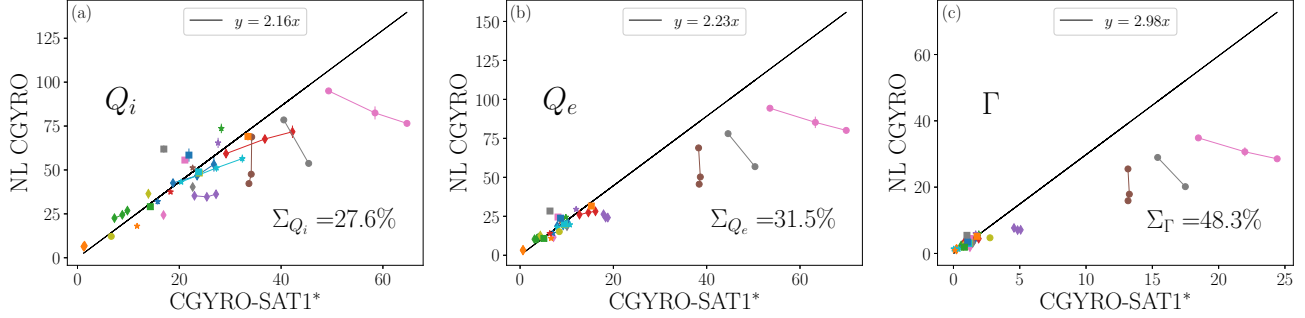

Figure 18: Scatter plots equivalent to those of figure 17, however now comparing NL CGYRO against CGYRO-SAT1* results for (a) ion energy flux, (b) electron energy flux and (c) particle flux. The rescaling constants for the different flux types are displayed in the legends.

A selection of energy flux scans with various key tokamak parameters is shown in figure 20, comparing NL CGYRO and CGYRO-SAT3. The density gradient scan is a recreation of a subset of the data points from figure 1, now with larger NL CGYRO fluxes, demonstrating the recreation of the positive isotope scaling for the ITG-dominated GA-std cases at low density gradient, the grouping of the fluxes for the transition case, and the anti-gyroBohm scaling at the high density gradient TEM-dominated $a/L_n = 3.0$ case. How this $a/L_n = 3.0$ case varies with collisionality is then displayed in figure 20(b), from which it is seen that the correct scaling is maintained across a large range of collisionalities. Finally the ion and electron heat fluxes against matched temperature gradients ($a/L_{T_i} = a/L_{T_e}$) are shown in figure 20(c). The general trend in both isotope scaling and magnitude can be observed to agree with the NL CGYRO data, however the fluxes appear to be somewhat under-predicted near the point of threshold. The generality of SAT3's behaviour in this region presents an area to be investigated further, as this is a key region of parameter space for experimental conditions.

To connect these results with the observations made in Section 4, figure 21 shows a recreation of figure 3(b), exhibiting the isotope scaling of the ion energy flux components Q_{i,k_y} in the $a/L_n = 3.0$ case for the different models,
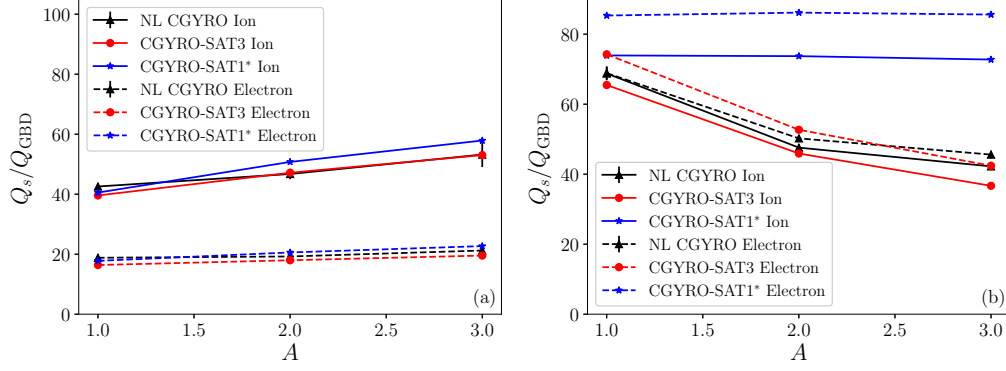
Figure 19: Turbulent ion energy fluxes (solid lines) and electron energy fluxes (dashed lines) against isotope mass for NL CGYRO (black), CGYRO-SAT3 (red) and CGYRO-SAT1* (blue), for the ITG-dominated GA-standard case (a) and the TEM-dominated $a/L_n = 3.0$ case (b). Note the recreation of the anti-gyroBohm scaling seen in the $a/L_n = 3.0$ case for CGYRO-SAT3.
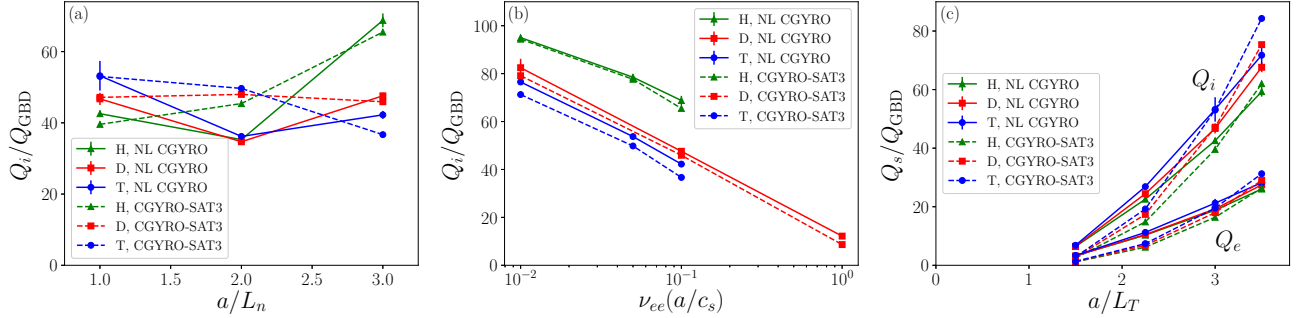

Figure 20: (a) Ion energy fluxes for NL CGYRO (solid lines) and CGYRO-SAT3 (dashed lines) against density gradient scale length a/L_n. (b) Ion energy fluxes for NL CGYRO and CGYRO-SAT3 against collisionality, keeping $a/L_n = 3.0$ fixed. (c) Ion and electron energy fluxes for NL CGYRO and CGYRO-SAT3 against matched temperature gradient scale length, $a/L_{T_i} = a/L_{T_e}$.

now with the data for CGYRO-SAT3 included. The improved low $k_y \rho_i$ variation and offset in the isotope scaling can be seen, as a consequence of the strong spectral shape and the differing TEM saturation level in SAT3.
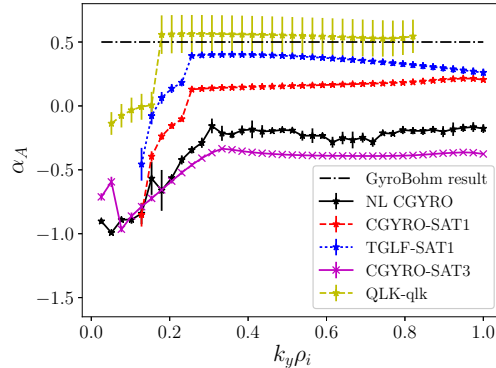

Figure 21: Isotope scaling metric α_A of the flux components for the $a/L_n = 3.0$ case, for NL CGYRO (black), CGYRO-SAT3 (purple), CGYRO-SAT1 (red), TGLF-SAT1 (blue) and QuaLiKiz-qlk (yellow). The error bars shown for all models are the uncertainties in the fitted parameter α_A.

6.1 A note on future improvements

The SAT3 model presented above is an accurate model for the enhanced CGYRO database generated, and is promising for extrapolation within the most common ITG and TEM turbulence regimes found in experiment. It does not however represent a complete description of turbulent plasma transport, and will of course perform less reliably in a parameter space far from its training database. The approach taken in SAT3's development however naturally presents a methodology with which to diagnose and improve on such future discrepancies. That is, for some hypothetical simulation that this model catastrophically fails to recreate, an established methodology can be employed to effectively diagnose and attempt to rectify the issue.

This approach starts by taking care to preserve the role of each physical element that constitutes the model flux calculation, so as to keep separate the contributions of the QLA, the weights, and the potentials. This decomposition of the reduced model clarifies which aspect of the reduced model is responsible for the recreation of each part of the nonlinear flux, and each can be considered in turn when attempting to diagnose future model disagreements with NL gyrokinetic results.

If the discrepancy is found to originate in the saturation rule, then one can first test whether the underlying functional relations (equations 19 and 20) still hold when their parameters are fitted to nonlinear data. If not, these will need to be amended. Otherwise, one continues to the question of the linear modelling of the parameters c_1, $k_{\min}$, c/b and $\left\langle \left| \delta\hat{\phi}_{k_y=k_0} \right|^2 \right\rangle_{x,\theta,t} / \Delta k_y$, each of which can be considered modularly. If a more robust method for approximating $k_{\min}$ from the linear data is discovered in the future for example, one can replace/amend that aspect of the model without requiring change elsewhere.

7 Conclusion

The isotope scaling of fluxes in local nonlinear gyrokinetics and quasilinear models has been considered. It was confirmed that existing quasilinear models generally struggle to capture the isotope scaling of fluxes seen in nonlinear gyrokinetic simulations, in part due to the historical lack of focus on isotopes other than deuterium in the development of their saturation rules and an incomplete understanding of the isotope effect. The origin of this non-trivial isotope scaling in nonlinear gyrokinetics was demonstrated to originate primarily in the magnitude of the saturated electrostatic potentials, with current quasilinear models failing to replicate this behaviour due to missing one or both of the following effects in their saturation rules: the variation in the isotope scaling with k_y in the low-k_y region, and the 'offset' from the gyroBohm-predicted level, which is sensitive to the dominant mode type.

In developing a new saturation rule to capture this behaviour the general form of the 2D potential spectrum in k_x and k_y was first considered, generalising the previous assumption of a squared Lorentzian form. The 2D model adhered to the data extremely well across a range of decades in radial wavenumber.

The new 1D saturation model SAT3 was then developed on a database of 43 simulations, including both ITG- and TEM-dominated cases. This database is similar in scope to those used for previous TGLF saturation models, however now includes simulations in different isotopes. A summary of the SAT3 model is given in Section 5.7. An accurate model for the spectral shape was built using a robust novel relationship between the 1D potentials $\left\langle \left| \delta\hat{\phi}_{k_y} \right|^2 \right\rangle_{x,\theta,t} / \Delta k_y$ and the radial spectral widths σ_{k_y} that was discovered in the NL gyrokinetic simulation results, which appears to capture a conserved quantity in electrostatic turbulence. The resulting parameters of SAT3, $k_{\min}, c/b, c_1$ and $\left\langle \left| \delta\hat{\phi}_{k_y=k_0} \right|^2 \right\rangle_{x,\theta,t} / \Delta k_y$ were modelled using linear quantities inspired from a previous work. The database demonstrated different saturation levels for ITG and TEM turbulence, which motivated a saturation model for each mode type with a transition function between them. The QLA functions were considered explicitly, however ultimately constant factors to discriminate between mode type and moment were used.

The new model has been shown to better capture the isotope scaling of the cases in the database, particularly in the cases of TEM-dominated turbulence, whilst performing at least as well as existing quasilinear models in other parameters, as exhibited via comparison with CGYRO-SAT1* in figures 17 and 18. Generalisations of the model outside of the dataset have been implemented, namely the effect of $E \times B$ shear and multi-ion plasma operation. Having been constructed from a database of predominantly ion-scale, electrostatic core plasmas, dominated by either

ITG or TEM turbulence, SAT3's applicability is naturally most valid in these regions of parameter space. Caution should therefore be exercised in the use of SAT3 away from these areas, such as plasmas for which electromagnetic effects or electron-scale dynamics are expected to be significant, in the pedestal, or in the presence of dominant modes other than the ITG or TEM. Generalisation of SAT3 into these regimes will require comparison to additional nonlinear gyrokinetic simulations. An algorithm for performing such generalisations, based on the systematic comparison of the constituent parts of SAT3 to nonlinear gyrokinetic data, is discussed in Section 6.1.

In future work SAT3 will be paired with the linear solvers of TGLF and QuaLiKiz for use in integrated modelling suites, to be validated against experimental data from recent isotope campaigns on JET and other machines. Whilst a degree of error will be incurred in flux prediction by moving from an exact linear solver to a fast linear solver, this effect is expected to be small, with fast linear solvers having shown good agreement with linear gyrokinetics in the most common experimentally-relevant regimes [28].

8   Acknowledgements

9   Appendices

A   Geometry and averages

The field-aligned coordinate system used in this work $\{x, y, \theta\}$ is defined such that the equilibrium magnetic field can be expressed

$$\mathbf{B} = B_{\text{unit}} \nabla x \times \nabla y = \frac{B_{\text{unit}}}{\mathcal{J}_{xy\theta}} \mathbf{a}_\theta \tag{A.1}$$

where $\mathcal{J}_{xy\theta}$ is the Jacobian of the field-aligned system and $\mathbf{a}_\theta$ is the covariant basis vector of the θ coordinate. Field lines are given by constant $\{x, y\}$ and θ measures the distance along a field line. These coordinates are equivalent to $x = r'$, $y = -r_0 \alpha'/q(r_0)$ and $\theta = -\theta'$, where dashed coordinates are those defined by CGYRO [9], with r_0 being the reference flux-surface.

Fluctuating quantities can be written as a Fourier series in the perpendicular-to-field coordinates x and y,

$$\delta f(x, y, \theta, t) = \sum_{k_x} \sum_{k_y} \delta \hat{f}_{k_x, k_y}(\theta, t) e^{ik_x x} e^{ik_y y} \tag{A.2}$$

where $k_x = 2\pi n_x / L_x$ and $k_y = 2\pi n_y / L_y$. The radial domain length L_x is quantised due to the parallel periodicity condition such that $L_x = L_y w / (2\pi \hat{s})$ for box size integer w.

Averages over the radial, binormal and parallel directions are defined by

$$\langle f \rangle_x = \frac{1}{L_x} \int_{x_0}^{x_0 + L_x} f \, \mathrm{d}x \tag{A.3}$$

$$\langle f \rangle_y = \frac{1}{L_y} \int_{y_0}^{y_0 + L_y} f \, \mathrm{d}y \tag{A.4}$$

$$\langle f \rangle_\theta = \frac{\int_{-\pi}^{\pi} f \mathcal{J}_{xy\theta}(\theta) \, \mathrm{d}\theta}{\int_{-\pi}^{\pi} \mathcal{J}_{xy\theta}(\theta) \, \mathrm{d}\theta} \tag{A.5}$$

where x_0 and y_0 are the lower bounds of the x and y domains. The time average is given by

$$\langle f \rangle_t = \frac{1}{\Delta t} \int_{t_0}^{t_0 + \Delta t} f \, dt \tag{A.6}$$

for some initial time t_0. Here $\Delta t = \tau - t_0$, where τ is the upper bound of the time domain. Equation A.6 is equivalent to taking the mean of 3 time-window averages of length $\Delta t / 3$ over the same domain, the methodology discussed in section 3, by virtue of

$$\frac{1}{\Delta t} \int_{t_0}^{t_0 + \Delta t} f \, dt = \frac{1}{N} \sum_{j=1}^{N} \frac{1}{(\Delta t / N)} \int_{t_0 + (j-1)(\Delta t / N)}^{t_0 + j(\Delta t / N)} f \, dt \tag{A.7}$$

for any integer N.

In the local limit, the combination of an ensemble average and a flux-surface average amounts to an average over the three spatial dimensions plus time

$$\langle f \rangle_{\text{Ens,FS}} = \langle f \rangle_{x,y,\theta,t}. \tag{A.8}$$

Angular brackets without a subscript denote a type of averaging weighted over the potential magnitudes, used in equations 4 and 12.

$$\langle f \rangle = \frac{\sum_{k_x} \left\langle f \left| \delta \hat{\phi}_{k_x,k_y} \right|^2 \right\rangle_{\theta,t}}{\left\langle \left| \delta \hat{\phi}_{k_y} \right|^2 \right\rangle_{x,\theta,t}} \tag{A.9}$$

B   Turbulent flux calculation

This section provides a step-by-step derivation of equation 2, taking equation 1 as the starting point. Evaluating equation 1 in the field-aligned system, one obtains

$$Q_s = -\left\langle \frac{1}{B_{\text{unit}}} \delta p_s \frac{\partial \delta \phi}{\partial y} \right\rangle_{\text{Ens,FS}}. \tag{B.1}$$

Inserting the Fourier representation from equation A.2 for the potential and pressure fluctuations and using equation A.8, equation B.1 becomes

$$Q_s = \left\langle \sum_{k_x} \sum_{k_x'} \sum_{k_y} \sum_{k_y'} \frac{-i k_y'}{B_{\text{unit}}} \delta \hat{p}_{s,k_x,k_y}(\theta,t) \, \delta \hat{\phi}_{k_x',k_y'}(\theta,t) \, e^{i(k_x + k_x')x} e^{i(k_y + k_y')y} \right\rangle_{x,y,\theta,t}. \tag{B.2}$$

Upon carrying out the averages in x and y, the orthogonality of the exponentials leaves only the terms with $k_x' = -k_x$, $k_y' = -k_y$:

$$Q_s = \sum_{k_x} \sum_{k_y} \frac{i k_y}{B_{\text{unit}}} \left\langle \delta \hat{p}_{s,k_x,k_y}(\theta,t) \, \delta \hat{\phi}_{-k_x,-k_y}(\theta,t) \right\rangle_{\theta,t}. \tag{B.3}$$

Because the quantities involved in this calculation are real, their Fourier components satisfy $\delta \hat{f}_{-k_x,-k_y} = \delta \hat{f}_{k_x,k_y}^*$, which when applied to the potentials gives

$$Q_s = \sum_{k_x} \sum_{k_y} \frac{i k_y}{B_{\text{unit}}} \left\langle \delta \hat{p}_{s,k_x,k_y}(\theta,t) \, \delta \hat{\phi}_{k_x,k_y}^*(\theta,t) \right\rangle_{\theta,t} = \sum_{k_x} \sum_{k_y} V_{k_x,k_y} \tag{B.4}$$

where $V_{k_x k_y}$ has been introduced to reduce clutter in the following. Observing $V_{k_x,k_y=0} = 0$, equation B.4 may be written

$$Q_s = \sum_{k_y > 0} \sum_{k_x} \left(V_{k_x,k_y} + V_{k_x,-k_y} \right). \tag{B.5}$$

Using the result $\sum_{k_x} V_{k_x,-k_y} = \sum_{k_x} V_{-k_x,-k_y}$, as well as the property $V_{k_x,k_y}^* = V_{-k_x,-k_y}$:

$$Q_s = \sum_{k_y > 0} \sum_{k_x} \left(V_{k_x,k_y} + V_{-k_x,-k_y} \right) = \sum_{k_y > 0} \sum_{k_x} \left(V_{k_x,k_y} + V_{k_x,k_y}^* \right). \tag{B.6}$$

This may be expressed more succinctly using the definition of the real part of a complex number, $\text{Re}\,[z] = (z + z^*)\,/2$:

$$Q_s = 2 \sum_{k_y>0} \sum_{k_x} \text{Re}\,\left[V_{k_x k_y}\right]. \tag{B.7}$$

Here the real property of the fields has introduced a symmetry to the terms, such that the flux contribution from the negative binormal modes is equal to that of the positive. Re-writing equation B.7 using $\text{Re}\,[iz] = -\text{Im}\,[z] = \text{Im}\,[z^*]$ gives

$$Q_s = 2 \sum_{k_y>0} \sum_{k_x} \frac{k_y}{B_{\text{unit}}} \left\langle \text{Im}\,\left[\delta\hat{p}^*_{s,k_x,k_y}\,(\theta,t)\,\delta\hat{\phi}_{k_x,k_y}\,(\theta,t)\right] \right\rangle_{\theta,t}. \tag{B.8}$$

In order to express the right-hand side of equation B.8 in terms of the magnitude of the electrostatic potentials and the phase difference between the fluctuations, one can define Z_{s,k_x,k_y} such that for every Fourier mode $\delta\hat{p}_{s,k_x,k_y} = Z_{s,k_x,k_y}\delta\hat{\phi}_{k_x,k_y}$. Multiplying both sides of this relation by $\delta\hat{\phi}^*_{k_x,k_y}$, taking the complex conjugate and isolating the imaginary part yields $\text{Im}\,\left[\delta\hat{p}^*_{s,k_x,k_y}\,(\theta,t)\,\delta\hat{\phi}_{k_x,k_y}\,(\theta,t)\right] = \text{Im}\,\left[Z^*_{s,k_x,k_y}\right]\left|\delta\hat{\phi}_{k_x,k_y}\right|^2$. The total flux may therefore finally be written

$$Q_s = 2 \sum_{k_y>0} \sum_{k_x} \frac{k_y}{B_{\text{unit}}} \left\langle \text{Im}\,\left[Z^*_{s,k_x,k_y}\right]\left|\delta\hat{\phi}_{k_x,k_y}\right|^2 \right\rangle_{\theta,t} \tag{B.9}$$

which is equation 2.

C   Parseval's theorem

Parseval's theorem relates the average of an absolute squared function in real space to the sum of the absolute squares of its Fourier amplitudes. Consider the Fourier representation of a function $f(x)$ over a finite domain $\{x_0, x_0 + L\}$

$$f(x) = \sum_{k_x} \hat{f}_{k_x} e^{ik_x x} \tag{C.1}$$

where $k_x = 2\pi n_x/L$ for all integers n_x. Multiplying both sides by $f^*(x)$ and averaging over the domain leaves only the $k_x = k'_x$ terms, producing the result.

$$\frac{1}{L}\int_{x_0}^{x_0+L} |f(x)|^2 \; \text{d}x = \sum_{k_x} \sum_{k'_x} \hat{f}_{k_x}\hat{f}^*_{k'_x}\frac{1}{L}\int_{x_0}^{x_0+L} e^{i\left(k_x-k'_x\right)x}\,\text{d}x$$
$$= \sum_{k_x}\left|\hat{f}_{k_x}\right|^2 \tag{C.2}$$

D   Grid-resolution dependence

The flux Q_s in equation 2 is a physical quantity, resulting in part from a spatial average over the x and y domains. It should therefore be independent of the binormal wavenumber grid resolution Δk_y, once past a certain value required for convergence. It then follows that the flux components Q_{s,k_y} must depend on the grid resolution, as if one doubles the resolution, one doubles the number of terms in the sum while maintaining a constant total.

Multiplying and dividing the right-hand side of equation 2 by Δk_y and approximating the summation as an integral gives

$$Q_s = \sum_{k_y>0} \frac{Q_{s,k_y}}{\Delta k_y}\Delta k_y \approx \int_0^\infty \frac{Q_{s,k_y}}{\Delta k_y}\,\text{d}k_y \tag{D.1}$$

and thus because the area under $Q_{s,k_y}/\Delta k_y$ is independent of the grid resolution, so too must $Q_{s,k_y}/\Delta k_y$ be itself. Analogously for the potentials, the volume and time average of the squared potentials in real space must be independent of Δk_y. Using Parseval's theorem,

$$\left\langle |\delta\phi|^2\right\rangle_{x,y,\theta,t} = \sum_{k_y}\left\langle \left|\delta\hat{\phi}_{k_y}\right|^2\right\rangle_{x,\theta,t} \tag{D.2}$$

it follows that

$$\left\langle |\delta\phi|^2 \right\rangle_{x,y,\theta,t} \approx \int_{-\infty}^{\infty} \frac{\left\langle \left|\delta\hat\phi_{k_y}\right|^2 \right\rangle_{x,\theta,t}}{\Delta k_y}\, \mathrm{d}k_y \tag{D.3}$$

and therefore $\left\langle \left|\delta\hat\phi_{k_y}\right|^2 \right\rangle_{x,\theta,t} /\Delta k_y$ must also be independent of Δk_y. Now using equation 5, one finds

$$\frac{\left\langle \left|\delta\hat\phi_{k_y}\right|^2 \right\rangle_{x,\theta,t}}{\Delta k_y} = \sum_{k_x} \frac{\left\langle \left|\delta\hat\phi_{k_x,k_y}\right|^2 \right\rangle_{\theta,t}}{\Delta k_y \Delta k_x}\Delta k_x \approx \int_{-\infty}^{\infty} \frac{\left\langle \left|\delta\hat\phi_{k_x,k_y}\right|^2 \right\rangle_{\theta,t}}{\Delta k_y \Delta k_x}\, \mathrm{d}k_x \tag{D.4}$$

resulting in $\left\langle \left|\delta\hat\phi_{k_x,k_y}\right|^2 \right\rangle_{\theta,t} /\Delta k_y \Delta k_x$ being the grid-independent version of the 2D potentials.

E   2D spectrum moment integrals

Here the first three moments of the 2D potential spectrum (equations 5, 12 and 13) are integrated analytically to obtain expressions for the coefficients C_1, C_2 and K in equation 11. Starting with the zeroth moment, defined by equation 5, then by approximating the summation as an integral and inserting equation 11 for the 2D potential spectrum, one obtains

$$\left\langle \left|\delta\hat\phi_{k_y}\right|^2 \right\rangle_{x,\theta,t} = \frac{1}{\Delta k_x}\int_{-\infty}^{\infty} \frac{\left\langle \left|\delta\hat\phi_{k_x=K,k_y}\right|^2 \right\rangle_{\theta,t}}{1 + C_1\,(k_x - K)^2 + C_2\,(k_x - K)^4}\, \mathrm{d}k_x. \tag{E.1}$$

Taking out a factor of C_2 from the denominator, the integral may be written

$$\left\langle \left|\delta\hat\phi_{k_y}\right|^2 \right\rangle_{x,\theta,t} = D\int_{-\infty}^{\infty} \frac{1}{E + Fu^2 + u^4}\, \mathrm{d}u \tag{E.2}$$

where $D = \left\langle \left|\delta\hat\phi_{k_x=K,k_y}\right|^2 \right\rangle_{\theta,t} /(C_2\Delta k_x)$, $E = 1/C_2$, $F = C_1/C_2$ and $u = k_x - K$. The denominator can then be factorised via $E + Fu^2 + u^4 = \left(u^2 + G\right)\left(u^2 + H\right)$, where $G = \frac{1}{2}\left(F + \sqrt{F^2 - 4E}\right)$, $H = \frac{1}{2}\left(F - \sqrt{F^2 - 4E}\right)$ and $F = G + H$, $E = GH$. Note that for the integral to have no singularities one requires $G, H > 0$, and hence $E, F > 0$. This factorised form can then be separated using partial fractions as

$$\left\langle \left|\delta\hat\phi_{k_y}\right|^2 \right\rangle_{x,\theta,t} = \frac{D}{G - H}\int_{-\infty}^{\infty}\left[\frac{1}{u^2 + H} - \frac{1}{u^2 + G}\right]\, \mathrm{d}u. \tag{E.3}$$

Using the substitution $u = \sqrt{H}\tan(v)$ and $u = \sqrt{G}\tan(v)$ respectively for the two integrals, equation E.3 evaluates to

$$\begin{aligned}
\left\langle \left|\delta\hat\phi_{k_y}\right|^2 \right\rangle_{x,\theta,t} &= \frac{D}{G - H}\left[\frac{1}{\sqrt{H}}\arctan\left(\frac{u}{\sqrt{H}}\right) - \frac{1}{\sqrt{G}}\arctan\left(\frac{u}{\sqrt{G}}\right)\right]_{-\infty}^{\infty} \\
&= \frac{D\pi}{\sqrt{GH}\left(\sqrt{G} + \sqrt{H}\right)}.
\end{aligned} \tag{E.4}$$

Squaring this equation, using the relations $GH = 1/C_2$, $G + H = C_1/C_2$ and re-arranging, one finds

$$C_1 + 2\sqrt{C_2} = \left(\frac{\pi\left\langle \left|\delta\hat\phi_{k_x=K,k_y}\right|^2 \right\rangle_{\theta,t}}{\Delta k_x \left\langle \left|\delta\hat\phi_{k_y}\right|^2 \right\rangle_{x,\theta,t}}\right)^2. \tag{E.5}$$

Turning now to the first moment, equation 12, this can be found via

$$
\begin{aligned}
\langle k_x \rangle &= \frac{\sum_{k_x} (u + K) \left\langle \left| \delta\hat{\phi}_{k_x,k_y} \right|^2 \right\rangle_{\theta,t}}{\left\langle \left| \delta\hat{\phi}_{k_y} \right|^2 \right\rangle_{x,\theta,t}} \\
&= \frac{\sum_{k_x} u \left\langle \left| \delta\hat{\phi}_{k_x,k_y} \right|^2 \right\rangle_{\theta,t}}{\left\langle \left| \delta\hat{\phi}_{k_y} \right|^2 \right\rangle_{x,\theta,t}} + K \\
&= \frac{D}{\left\langle \left| \delta\hat{\phi}_{k_y} \right|^2 \right\rangle_{x,\theta,t}} \left[\int_{-\infty}^{\infty} \frac{u}{E + Fu^2 + u^4} \, du \right] + K \\
&= K
\end{aligned}
\tag{E.6}
$$

as the integral of an odd function over a symmetric boundary is zero.

The second moment, equation 13, can be written

$$
\sigma_{k_y}^2 = \frac{D}{\left\langle \left| \delta\hat{\phi}_{k_y} \right|^2 \right\rangle_{x,\theta,t}} \int_{-\infty}^{\infty} \frac{u^2}{E + Fu^2 + u^4} \, du
\tag{E.7}
$$

which, following an analogous method of solution as the zeroth moment, evaluates to

$$
\begin{aligned}
\sigma_{k_y}^2 &= \frac{1}{\left\langle \left| \delta\hat{\phi}_{k_y} \right|^2 \right\rangle_{x,\theta,t}} \frac{D}{G - H} \int_{-\infty}^{\infty} \left[\frac{G}{u^2 + G} - \frac{H}{u^2 + H} \right] du \\
&= \frac{1}{\left\langle \left| \delta\hat{\phi}_{k_y} \right|^2 \right\rangle_{x,\theta,t}} \frac{D}{G - H} \left[\sqrt{G} \arctan\left(\frac{u}{\sqrt{G}} \right) - \sqrt{H} \arctan\left(\frac{u}{\sqrt{H}} \right) \right]_{-\infty}^{\infty} \\
&= \frac{1}{\left\langle \left| \delta\hat{\phi}_{k_y} \right|^2 \right\rangle_{x,\theta,t}} \frac{D\pi}{\sqrt{G} + \sqrt{H}}.
\end{aligned}
\tag{E.8}
$$

Squaring this result and expressing it in terms of C_1 and C_2 gives

$$
C_2 \left(C_1 + 2\sqrt{C_2} \right) = \left(\frac{\pi \left\langle \left| \delta\hat{\phi}_{k_x = \langle k_x \rangle, k_y} \right|^2 \right\rangle_{\theta,t}}{\Delta k_x \left\langle \left| \delta\hat{\phi}_{k_y} \right|^2 \right\rangle_{x,\theta,t}} \right)^2 \frac{1}{\sigma_{k_y}^4}
\tag{E.9}
$$

which when combined with equation E.5, produces the desired solutions

$$
C_2 = \frac{1}{\sigma_{k_y}^4}, \qquad C_1 = \left[\left(\frac{\pi \left\langle \left| \delta\hat{\phi}_{k_x = \langle k_x \rangle, k_y} \right|^2 \right\rangle_{\theta,t} \sigma_{k_y}}{\Delta k_x \left\langle \left| \delta\hat{\phi}_{k_y} \right|^2 \right\rangle_{x,\theta,t}} \right)^2 - 2 \right] \frac{1}{\sigma_{k_y}^2}.
\tag{E.10}
$$

The results of this section have been derived assuming integration over the entire k_x domain, which is inaccessible for turbulence simulations. For some finite domain $\{-k_{x,\text{lim}}, k_{x,\text{lim}}\}$, these results continue to hold provided that $k_{x,\text{lim}} \gg |\langle k_x \rangle| + \sigma_{k_y}$.

References

[1] Staebler GM, Belli EA, Candy J, Kinsey JE, Dudding H, Patel B. Verification of a quasi-linear model for gyrokinetic turbulent transport. Nuclear Fusion. 2021 Sep;61(11):116007. Publisher: IOP Publishing. Available from: https://doi.org/10.1088/1741-4326/ac243a.

[2] Bessenrodt-Weberpals M, Wagner F, Gehre O, Giannone L, Hofmann JV, Kallenbach A, et al. The isotope effect in ASDEX. Nuclear Fusion. 1993 Aug;33(8):1205-38. Publisher: IOP Publishing. Available from: https://doi.org/10.1088/0029-5515/33/8/i09.

[3] Schneider PA, Bustos A, Hennequin P, Ryter F, Bernert M, Cavedon M, et al. Explaining the isotope effect on heat transport in L-mode with the collisional electron-ion energy exchange. Nuclear Fusion. 2017 Apr;57(6):066003. Publisher: IOP Publishing. Available from: https://doi.org/10.1088/1741-4326/aa65b3.

[4] Maggi CF, Weisen H, Hillesheim JC, Chankin A, Delabie E, Horvath L, et al. Isotope effects on L-H threshold and confinement in tokamak plasmas. Plasma Physics and Controlled Fusion. 2017 Nov;60(1):014045. Publisher: IOP Publishing. Available from: https://doi.org/10.1088/1361-6587/aa9901.

[5] Weisen H, Maggi CF, Oberparleiter M, Casson FJ, Camenen Y, Menmuir S, et al. Isotope dependence of energy, momentum and particle confinement in tokamaks. Journal of Plasma Physics. 2020 Oct;86(5). Publisher: Cambridge University Press. Available from: https://www.cambridge.org/core/journals/journal-of-plasma-physics/article/isotope-dependence-of-energy-momentum-and-particle-confinement-in-tokamaks/A24259BC335460AC4B0D7EFACE6068E4.

[6] ITER Physics Basis Expert Groups on Confinement and Transport and Confinement Modelling and Database, ITER Physics Basis Editors. Chapter 2: Plasma confinement and transport;39(12):2175-249. Publisher: IOP Publishing. Available from: https://doi.org/10.1088/0029-5515/39/12/302.

[7] Scott SD, Zarnstorff MC, Barnes CW, Bell R, Bretz NL, Bush C, et al. Isotopic scaling of confinement in deuterium–tritium plasmas. Physics of Plasmas. 1995 Jun;2(6):2299-307. Publisher: American Institute of Physics. Available from: https://aip.scitation.org/doi/10.1063/1.871253.

[8] Peeters AG, Camenen Y, Casson FJ, Hornsby WA, Snodin AP, Strintzi D, et al. The nonlinear gyro-kinetic flux tube code GKW. Computer Physics Communications. 2009 Dec;180(12):2650-72. Available from: https://www.sciencedirect.com/science/article/pii/S0010465509002112.

[9] Candy J, Belli EA, Bravenec RV. A high-accuracy Eulerian gyrokinetic solver for collisional plasmas. Journal of Computational Physics. 2016 Nov;324:73-93. Available from: https://www.sciencedirect.com/science/article/pii/S0021999116303400.

[10] Candy J, Belli EA. Gyro Technical Guide. General Atomics; 2011.

[11] Garcia J, Dumont RJ, Joly J, Morales J, Garzotti L, Bache TW, et al. First principles and integrated modelling achievements towards trustful fusion power predictions for JET and ITER. Nuclear Fusion. 2019 Aug;59(8):086047. Available from: https://iopscience.iop.org/article/10.1088/1741-4326/ab25b1.

[12] Manfredi G, Ottaviani M. Gyro-Bohm Scaling of Ion Thermal Transport from Global Numerical Simulations of Ion-Temperature-Gradient-Driven Turbulence. Physical Review Letters. 1997 Nov;79(21):4190-3. Publisher: American Physical Society. Available from: https://link.aps.org/doi/10.1103/PhysRevLett.79.4190.

[13] Belli EA, Candy J, Waltz RE. Reversal of turbulent gyroBohm isotope scaling due to nonadiabatic electron drive. Physics of Plasmas. 2019 Aug;26(8):082305. Publisher: American Institute of Physics. Available from: https://aip.scitation.org/doi/10.1063/1.5110401.

[14] Garcia J, Görler T, Jenko F, Giruzzi G. Gyrokinetic nonlinear isotope effects in tokamak plasmas. Nuclear Fusion. 2016 Dec;57(1):014007. Publisher: IOP Publishing. Available from: https://doi.org/10.1088/1741-4326/57/1/014007.

[15] Nakata M, Nunami M, Sugama H, Watanabe TH. Isotope Effects on Trapped-Electron-Mode Driven Turbulence and Zonal Flows in Helical and Tokamak Plasmas. Physical Review Letters. 2017 Apr;118(16):165002. Publisher: American Physical Society. Available from: https://link.aps.org/doi/10.1103/PhysRevLett.118.165002.

[16] Pusztai I, Candy J, Gohil P. Isotope mass and charge effects in tokamak plasmas. Physics of Plasmas. 2011 Dec;18(12):122501. Publisher: American Institute of Physics. Available from: `https://aip.scitation.org/doi/10.1063/1.3663844`.

[17] Bustos A, Bañón Navarro A, Görler T, Jenko F, Hidalgo C. Microturbulence study of the isotope effect. Physics of Plasmas. 2015 Jan;22(1):012305. Publisher: American Institute of Physics. Available from: `https://aip.scitation.org/doi/full/10.1063/1.4905637`.

[18] Bonanomi N, Casiraghi I, Mantica P, Challis C, Delabie E, Fable E, et al. Role of fast ion pressure in the isotope effect in JET L-mode plasmas. Nuclear Fusion. 2019 Jul;59(9):096030. Publisher: IOP Publishing. Available from: `https://doi.org/10.1088/1741-4326/ab2d4f`.

[19] Garcia J, Casson FJ, Bañón Navarro A, Bonanomi N, Citrin J, King D, et al. Modelling and theoretical understanding of the isotope effect from JET experiments in view of reliable predictions for deuterium-tritium plasmas. Plasma Physics and Controlled Fusion. 2022 May;64(5):054001. Available from: `https://iopscience.iop.org/article/10.1088/1361-6587/ac53ef`.

[20] Rhodes TL, Holland C, Smith SP, White AE, Burrell KH, Candy J, et al. L-mode validation studies of gyrokinetic turbulence simulations via multiscale and multifield turbulence measurements on the DIII-D tokamak. Nuclear Fusion. 2011 Jun;51(6):063022. Available from: `https://iopscience.iop.org/article/10.1088/0029-5515/51/6/063022`.

[21] Holland C, Schmitz L, Rhodes TL, Peebles WA, Hillesheim JC, Wang G, et al. Advances in validating gyrokinetic turbulence models against L- and H-mode plasmas. Physics of Plasmas. 2011 May;18(5):056113. Available from: `http://aip.scitation.org/doi/10.1063/1.3574518`.

[22] Told D, Jenko F, Görler T, Casson FJ, Fable E, ASDEX Upgrade Team. Characterizing turbulent transport in ASDEX Upgrade L-mode plasmas via nonlinear gyrokinetic simulations. Physics of Plasmas. 2013 Dec;20(12):122312. Available from: `http://aip.scitation.org/doi/10.1063/1.4858899`.

[23] Citrin J, Jenko F, Mantica P, Told D, Bourdelle C, Dumont R, et al. Ion temperature profile stiffness: non-linear gyrokinetic simulations and comparison with experiment. Nuclear Fusion. 2014 Feb;54(2):023008. Available from: `https://iopscience.iop.org/article/10.1088/0029-5515/54/2/023008`.

[24] Bonanomi N, Mantica P, Szepesi G, Hawkes N, Lerche E, Migliano P, et al. Trapped electron mode driven electron heat transport in JET: experimental investigation and gyro-kinetic theory validation. Nuclear Fusion. 2015 Sep;55(11):113016. Available from: `https://iopscience.iop.org/article/10.1088/0029-5515/55/11/113016`.

[25] Creely AJ, Howard NT, Rodriguez-Fernandez P, Cao N, Hubbard AE, Hughes JW, et al. Validation of nonlinear gyrokinetic simulations of L- and I-mode plasmas on Alcator C-Mod. Physics of Plasmas. 2017 May;24(5):056104. Available from: `http://aip.scitation.org/doi/10.1063/1.4977466`.

[26] Freethy SJ, Görler T, Creely AJ, Conway GD, Denk SS, Happel T, et al. Validation of gyrokinetic simulations with measurements of electron temperature fluctuations and density-temperature phase angles on ASDEX Upgrade. Physics of Plasmas. 2018 May;25(5):055903. Available from: `http://aip.scitation.org/doi/10.1063/1.5018930`.

[27] Citrin J, Maeyama S, Angioni C, Bonanomi N, Bourdelle C, Casson FJ, et al. Integrated modelling and multiscale gyrokinetic validation study of ETG turbulence in a JET hybrid H-mode scenario. Nuclear Fusion. 2022 Jun. Available from: `https://iopscience.iop.org/article/10.1088/1741-4326/ac7535`.

[28] Staebler GM, Kinsey JE, Waltz RE. Gyro-Landau fluid equations for trapped and passing particles. Physics of Plasmas. 2005 Oct;12(10):102508. Publisher: American Institute of Physics. Available from: `https://aip.scitation.org/doi/10.1063/1.2044587`.

[29] Bourdelle C, Citrin J, Baiocchi B, Casati A, Cottier P, Garbet X, et al. Core turbulent transport in toka-mak plasmas: bridging theory and experiment with QuaLiKiz. Plasma Physics and Controlled Fusion. 2015 Dec;58(1):014036. Publisher: IOP Publishing. Available from: `https://doi.org/10.1088/0741-3335/58/1/014036`.

[30] Stephens CD, Garbet X, Citrin J, Bourdelle C, van de Plassche KL, Jenko F. Quasilinear gyrokinetic theory: a derivation of QuaLiKiz. Journal of Plasma Physics. 2021 Aug;87(4):905870409. Available from: `https://www.cambridge.org/core/product/identifier/S0022377821000763/type/journal_article`.

[31] Staebler GM, Candy J, Howard NT, Holland C. The role of zonal flows in the saturation of multi-scale gyrokinetic turbulence. Physics of Plasmas. 2016 Jun;23(6):062518. Publisher: American Institute of Physics. Available from: `https://aip.scitation.org/doi/10.1063/1.4954905`.

[32] Casati A, Bourdelle C, Garbet X, Imbeaux F, Candy J, Clairet F, et al. Validating a quasi-linear transport model versus nonlinear simulations. Nuclear Fusion. 2009 Jul;49(8):085012. Publisher: IOP Publishing. Available from: `https://doi.org/10.1088/0029-5515/49/8/085012`.

[33] Citrin J, Bourdelle C, Casson FJ, Angioni C, Bonanomi N, Camenen Y, et al. Tractable flux-driven temperature, density, and rotation profile evolution with the quasilinear gyrokinetic transport model QuaLiKiz. Plasma Physics and Controlled Fusion. 2017 Dec;59(12):124005. Available from: `https://iopscience.iop.org/article/10.1088/1361-6587/aa8aeb`.

[34] Ho A, Citrin J, Auriemma F, Bourdelle C, Casson FJ, Kim HT, et al. Application of Gaussian process regression to plasma turbulent transport model validation via integrated modelling. Nuclear Fusion. 2019 Mar;59(5):056007. Publisher: IOP Publishing. Available from: `https://doi.org/10.1088/1741-4326/ab065a`.

[35] Casson FJ, Patten H, Bourdelle C, Breton S, Citrin J, Koechl F, et al. Predictive multi-channel flux-driven modelling to optimise ICRH tungsten control and fusion performance in JET. Nuclear Fusion. 2020 Jun;60(6):066029. Available from: `https://iopscience.iop.org/article/10.1088/1741-4326/ab833f`.

[36] Marin M, Citrin J, Garzotti L, Valovic M, Bourdelle C, Camenen Y, et al. Multiple-isotope pellet cycles captured by turbulent transport modelling in the JET tokamak. Nuclear Fusion. 2021 Mar;61(3):036042. Available from: `https://iopscience.iop.org/article/10.1088/1741-4326/abda00`.

[37] Waltz RE, Staebler GM, Dorland W, Hammett GW, Kotschenreuther M, Konings JA. A gyro-Landau-fluid transport model. Physics of Plasmas. 1997 Jul;4(7):2482-96. Publisher: American Institute of Physics. Available from: `https://aip.scitation.org/doi/citedby/10.1063/1.872228`.

[38] Beer MA, Cowley SC, Hammett GW. Field-aligned coordinates for nonlinear simulations of tokamak turbulence. Physics of Plasmas. 1995 Aug;2(7):2687-700. Publisher: American Institute of Physics. Available from: `https://aip.scitation.org/doi/abs/10.1063/1.871232`.

[39] Abel IG, Plunk GG, Wang E, Barnes M, Cowley SC, Dorland W, et al. Multiscale gyrokinetics for rotating tokamak plasmas: fluctuations, transport and energy flows. Reports on Progress in Physics. 2013 Oct;76(11):116201. Publisher: IOP Publishing. Available from: `https://doi.org/10.1088/0034-4885/76/11/116201`.

[40] Sugama H, Horton W. Nonlinear electromagnetic gyrokinetic equation for plasmas with large mean flows. Physics of Plasmas. 1998 Jul;5(7):2560-73. Publisher: American Institute of Physics. Available from: `https://aip.scitation.org/doi/10.1063/1.872941`.

[41] Dannert T, Jenko F. Gyrokinetic simulation of collisionless trapped-electron mode turbulence. Physics of Plasmas. 2005 Jul;12(7):072309. Available from: `http://aip.scitation.org/doi/10.1063/1.1947447`.

[42] Angioni C, Peeters AG, Jenko F, Dannert T. Collisionality dependence of density peaking in quasilinear gyrokinetic calculations. Physics of Plasmas. 2005 Nov;12(11):112310. Available from: `http://aip.scitation.org/doi/10.1063/1.2135283`.

[43] Casson FJ, McDermott RM, Angioni C, Camenen Y, Dux R, Fable E, et al. Validation of gyrokinetic modelling of light impurity transport including rotation in ASDEX Upgrade. Nuclear Fusion. 2013 Jun;53(6):063026. Available from: `https://iopscience.iop.org/article/10.1088/0029-5515/53/6/063026`.

[44] Patel B. Confinement physics for a steady state net electric burning spherical tokamak [phd]. University of York; 2021. Available from: `https://etheses.whiterose.ac.uk/28991/`.

[45] Waltz RE, Casati A, Staebler GM. Gyrokinetic simulation tests of quasilinear and tracer transport. Physics of Plasmas. 2009 Jul;16(7):072303. Available from: `http://aip.scitation.org/doi/10.1063/1.3167391`.

[46] Candy J. A unified method for operator evaluation in local Grad–Shafranov plasma equilibria. Plasma Physics and Controlled Fusion. 2009 Oct;51(10):105009. Available from: `https://iopscience.iop.org/article/10.1088/0741-3335/51/10/105009`.

[47] Peeters AG, Angioni C, Bortolon A, Camenen Y, Casson FJ, Duval B, et al. Overview of toroidal momentum transport. Nuclear Fusion. 2011 Aug;51(9):094027. Publisher: IOP Publishing. Available from: `https://doi.org/10.1088/0029-5515/51/9/094027`.

[48] Staebler GM, Waltz RE, Candy J, Kinsey JE. New Paradigm for Suppression of Gyrokinetic Turbulence by Velocity Shear. Physical Review Letters. 2013 Jan;110(5):055003. Publisher: American Physical Society. Available from: `https://link.aps.org/doi/10.1103/PhysRevLett.110.055003`.

[49] Casson FJ, Peeters AG, Camenen Y, Hornsby WA, Snodin AP, Strintzi D, et al. Anomalous parallel momentum transport due to E×B flow shear in a tokamak plasma. Physics of Plasmas. 2009 Sep;16(9):092303. Publisher: American Institute of Physics. Available from: `https://aip.scitation.org/doi/10.1063/1.3227650`.

[50] Cottier P, Bourdelle C, Camenen Y, Gürcan , Casson FJ, Garbet X, et al. Angular momentum transport modeling: achievements of a gyrokinetic quasi-linear approach. Plasma Physics and Controlled Fusion. 2014 Jan;56(1):015011. Available from: `https://iopscience.iop.org/article/10.1088/0741-3335/56/1/015011`.

[51] Citrin J, Bourdelle C, Cottier P, Escande DF, Gürcan , Hatch DR, et al. Quasilinear transport modelling at low magnetic shear. Physics of Plasmas. 2012 Jun;19(6):062305. Publisher: American Institute of Physics. Available from: `https://aip.scitation.org/doi/10.1063/1.4719697`.

[52] Lee WW, Krommes JA, Oberman CR, Smith RA. Nonlinear evolution of drift instabilities. The Physics of Fluids. 1984 Nov;27(11):2652-63. Publisher: American Institute of Physics. Available from: `https://aip.scitation.org/doi/10.1063/1.864567`.

[53] Merz F, Jenko F. Nonlinear interplay of TEM and ITG turbulence and its effect on transport. Nuclear Fusion. 2010 Apr;50(5):054005. Publisher: IOP Publishing. Available from: `https://doi.org/10.1088/0029-5515/50/5/054005`.